

**EROSION OF CONSOLIDATED COHESIVE BOTTOM
CONTAINING COHESIONLESS SEDIMENT
BY WAVE ACTION ON BEACH**

BY
TINGTING ZHU AND NOBUHISA KOBAYASHI

RESEARCH REPORT NO. CACR-19-01
MARCH 2019



CENTER FOR APPLIED COASTAL RESEARCH

University of Delaware
Newark, Delaware 19716

ACKNOWLEDGMENTS

This study was partially supported by the U.S. Army Corps of Engineers under Agreement No. W912HZ18P0134.

TABLE OF CONTENTS

LIST OF TABLES	iii
LIST OF FIGURES.....	iv
ABSTRACT	1
1 INTRODUCTION.....	2
2 SAND TRANSPORT MODEL ON ERODING COHESIVE BOTTOM.....	5
2.1 Cross-Shore Model (CSHORE)	5
2.2 Sand Volume Conservation Equation	6
2.3 Adjusted Dike Erosion Model.....	8
2.4 Computation Procedure	11
3 COMPARISON WITH AVAILABLE DATA	14
3.1 Till Erosion Experiment	14
3.2 Initial Profile and Input Parameters.....	19
3.3 Wave Hydrodynamics	22
3.4 Till Erosion Rates	26
4 APPLICATIONS OF NUMERICAL MODEL.....	34
4.1 Longer-Term Model Tests.....	34
4.2 Hypothetical Prototype Tests	41
4.3 Field Application	46
5 CONCLUSIONS	47
REFERENCES	49

LIST OF TABLES

Table 3.1	Spectral significant wave height H_{mo} and spectral peak period T_p for S75, S85, B75, and B85 tests.	16
Table 3.2	Input parameters to CSHORE for S75, S85, B75, and B85 tests.	20
Table 4.1	Deposited sand volume A_d , transported sand volume A_t , and sand volume A_e released by eroded till for duration of 100 h (Model) or 200 h (Prototype).....	36

LIST OF FIGURES

Figure 2.1	Definition sketch for sand surface elevation z_b and clay surface elevation z_p	6
Figure 2.2	Abrasion and protection function as a function of h_* with (a) $C_a = 0$, $C_p > 0$ and (b) $C_p = 0$, $C_a > 0$	10
Figure 2.3	Numerical scheme adopted in CSHORE of the computation from the given time t to the next time level $(t + \Delta t)$	12
Figure 3.1	Measured initial bottom profiles for S75 and S85 tests with different input values of R_c and f_c	17
Figure 3.2	Measured initial profiles for B75 and B85 tests in comparison to S75 and S85 profiles.....	18
Figure 3.2	Abrasion and protection function F with $C_a = 2$ and $C_p = 0.5$ as a function of normalized sand layer thickness h_*	21
Figure 3.4	Measured and computed ($\gamma = 0.6$ and 0.7 , $t = 1$ h) significant wave height H_{mo} for S75 and S85 tests.....	23
Figure 3.5	Measured and computed ($t = 1$ h and 10 h, $\gamma = 0.6$) significant wave height H_{mo} for S75 and S85 tests.....	23
Figure 3.6	Measured and computed ($\gamma = 0.6$ and 0.7 , $t = 1$ h) fraction Q of broken waves for S75 and S85 tests	24
Figure 3.7	Measured and computed ($t = 1$ h and 10 h, $\gamma = 0.6$) fraction Q of broken waves for S75 and S85 tests.....	24
Figure 3.8	Measured and computed ($\gamma = 0.6$ and 0.7 , $t = 1$ h) velocity standard deviation σ_u for S75 and S85 tests.....	25
Figure 3.9	Measured and computed ($t = 1$ h and 10 h, $\gamma = 0.6$) velocity standard deviation σ_u for S75 and S85 tests.....	25
Figure 3.10	Computed ($t = 1$ h and 10 h, $\gamma = 0.6$) sand movement probability P_b , sand layer thickness h_p and abrasion and protection function F as well as measured and computed erosion rates for S75 test.	28

Figure 3.11	Computed ($t = 1$ h and 10 h, $\gamma = 0.7$) P_b , h_p and F as well as measured and computed erosion rates for S75 test.	29
Figure 3.12	Computed ($t = 1$ h and 10 h, $\gamma = 0.6$) P_b , h_p and F as well as measured and computed erosion rates for S85 test.	30
Figure 3.13	Computed ($t = 1$ h and 10 h, $\gamma = 0.7$) P_b , h_p and F as well as measured and computed erosion rates for S85 test.	31
Figure 3.14	Measured and computed ($t = 1$ h and 10 h, $\gamma = 0.6$) erosion rates for B75 and B85 tests.....	32
Figure 3.15	Measured and computed ($t = 1$ h and 10 h, $\gamma = 0.7$) erosion rates for B75 and B85 tests.....	33
Figure 4.1	Sand surface elevation z_b and clay surface elevation z_p at $t = 0$ and 100 h for S75 and S85 tests.....	37
Figure 4.2	Computed sand layer thickness h_p at $t = 10, 50,$ and 100 h for S75 and S85 tests.....	38
Figure 4.3	Computed erosion rates at $t = 10, 50,$ and 100 h in comparison with measured erosion rate for S75 and S85 tests.....	38
Figure 4.4	Cross-shore bedload transport volume v_{bx} , suspended load transport volume v_{sx} , and net sand transport volume v_x (m^3/m) at $t = 10, 50,$ and 100 h for S75 test.....	39
Figure 4.5	Cross-shore sand transport volume v_{bx} , v_{sx} , and v_x (m^3/m) at $t = 10, 50,$ and 100 h for S85 test.....	40
Figure 4.6	Sand surface elevation z_b and clay surface elevation z_p at $t = 0$ and 200 h for S75P and S85P prototype tests	42
Figure 4.7	Computed sand layer thickness h_p at $t = 20, 100,$ and 200 for S75P and S85P prototype tests	43
Figure 4.8	Computed erosion rates at $t = 20, 100,$ and 200 for S75P and S85P prototype tests.....	43
Figure 4.9	Cross-shore sand transport volume v_{bx} , v_{sx} , and v_x (m^3/m) at $t = 20, 100,$ and 200 h for S75P prototype test	44

Figure 4.10 Cross-shore sand transport volume v_{bx} , v_{sx} , and v_x (m^3/m) at $t = 20$,
100, and 200 h for S85P prototype test 45

ABSTRACT

The erosion processes of consolidated cohesive sediment under irregular breaking waves are formulated to predict the profile evolution of a cohesive sediment beach with a layer of sand. The cohesive sediment is eroded by turbulence generated by wave energy dissipation caused by wave breaking and bottom friction. Sand released from the eroded sediment is transported onshore or offshore by wave action. The cohesive sediment erosion rate is increased by a thin mobile layer of sand and decreased by a thick sand layer. The complicated interactions of waves, sand and cohesive bottom are simplified and incorporated into an existing cross-shore numerical model. The model is compared with flume experiment data with measured till erosion rates of the order of 0.05 cm/h. The calibrated model is used to simulate the temporal change of the till erosion rate for the duration of 100 h. The scale effect is examined in hypothetical prototype tests of the same till with a length ratio of 1/4. The prototype 200-h simulations predict much larger till erosion near the shoreline and sand deposition in the surf zone. The model will need to be compared with actual field data.

Chapter 1

INTRODUCTION

A consolidated cohesive sediment layer exists below a layer of sand on some beaches (USACE 2003). A shore can be defined as consolidated cohesive when a cohesive sediment layer plays the dominant role in profile evolution and shore erosion. The erosion process of consolidated cohesive sediment may be gradual but irreversible (no recovery) apart from sand and gravel released from eroded consolidated cohesive sediment. Sand and gravel moving onshore or offshore by wave action can protect the underlying cohesive sediment bottom or serve as an abrasive agent, depending on its volume and wave energy. For glacial till shores along the Great Lakes, long-term bluff recession and beach erosion (down cutting) were observed to be correlated in order to maintain an equilibrium beach profile (Bishop et al. 1992; Kamphuis 1987).

Nairn and Southgate (1993) developed a numerical model to reproduce offshore bar formation on a thin sand layer overlaying a cohesive till substrate for a short duration of 1.25h. Empirical bluff erosion models were developed to predict the horizontal erosion (retreat) of soft rock (cohesive clay) shores [e.g., Walkden and Hall (2005); Trenhaile (2009)]. The cohesionless sediment transport processes on a shore platform were parameterized in these geomorphic models for the time scale of thousands of years unlike the sand transport model by Nairn and Southgate (1993). Beaches consisting of a thin veneer of sand on a cohesive sediment substrate are also common along the Gulf of Mexico where the backshore area is typically a salt marsh instead of a bluff. An experimental shore protection project consisting of a low volume beach fill and a clay core dune was carried out in Texas (Wamsley et al. 2011). No method exists for the design of a shore protection project based on locally available sand and clay.

Clay is also used for the construction of dikes (levees) [e.g., Wolters et al. 2008]. Kobayashi and Weitzner (2015) developed a dike erosion model to predict the temporal and cross-shore variations of vertical erosion depth on the seaward clay slope with or without a turf cover. The product of the erosion rate and the turf or clay resistance force was related to the rate of erosion work by turbulence generated by wave energy dissipation caused by wave breaking and bottom friction. The empirical parameters related to the turf and clay resistance were calibrated using available limited data of a prototype scale. The calibrated model reproduced the relation between the critical erosion velocity and duration of steady flow, the erosion rate on a seaward grassed slope, and the eroded profile evolution of a seaward clay slope. This dike erosion model was incorporated in the cross-shore numerical model CSHORE (Kobayashi 2016). CSHORE includes basic cohesionless sediment dynamics and has been shown to be applicable to small-scale and large-scale laboratory beaches as well as natural beaches.

In this study, the numerical model CSHORE is extended to predict erosion of a consolidated cohesive bottom containing cohesionless sediment under wave action. The limited availability of sand released from the eroding cohesive bottom is taken into account for the prediction of cross-shore sand transport rates. Chapter 2 explains this model and the governing equations in detail. The dike erosion model is adjusted to include the abrasive and protective effects of cohesionless sediment overlying on the cohesive bottom. A computation procedure is presented to predict hydrodynamics, profile evolution, and clay erosion rates. The sand budget in the computation domain is satisfied at each time step during the time marching computation because of the sensitivity of clay erosion to the overlying sand layer thickness.

Chapter 3 summarizes a small-scale laboratory flume experiment using intact till samples conducted by Bishop and Skafel (Bishop et al. 1992; Bishop and Skafel 1992; Skafel 1995; Skafel and Bishop 1994). The available laboratory data of wave hydrodynamic variables and erosion rates are compared with the extended CSHORE.

Chapter 4 describes the applications of the extended CSHORE for longer-term durations. The computation duration of two tests from Skafel (1995) is increased to 100 h. To examine scale effects, computation is also made of the corresponding two tests based on Froude similitude with a length ratio of 1/4 (model/prototype). Finally, additional efforts required for field applications are discussed briefly.

Chapter 2

SAND TRANSPORT MODEL ON ERODING COHESIVE BOTTOM

The cross-shore numerical model CSHORE is extended to include an option to incorporate sand transport and clay erosion in this chapter. The dike erosion model (Kobayashi and Weitzner 2015) is adjusted to include the abrasive and protective effects of sand particles on clay erosion in the numerical model CSHORE by Kobayashi (2016). A numerical scheme is developed to predict both clay bottom erosion and sand layer thickness at each time step.

2.1 Cross-Shore Model (CSHORE)

The components of CSHORE used in the subsequent computations for normally incident waves were as follows: a combined wave and current model based on time-averaged continuity, cross-shore momentum, wave energy, and roller energy equations; a cohesionless sediment (sand for brevity) transport model for suspended load and bedload; a continuity equation of sand bottom for beach profile evolution prediction; a probabilistic model for an intermittently wet and dry (swash) zone; and a dike erosion model for downward erosion of consolidated cohesive sediment (clay for brevity but it contains some cohesionless sediment).

Previous CSHORE applications were limited to sand transport on a fixed bottom and erosion of clay containing no sand. In this extended CSHORE, the continuity equation of sand bottom is modified to account for sand released from eroding clay

bottom. Erosion of clay bottom exposed to wave action is affected by overlaying sand particles (Kamphuis 1990). A thin mobile layer of sand particles increases clay erosion, whereas a thick sand layer protects underlying clay. The abrasive or protective effect of sand on clay erosion is taken into account empirically.

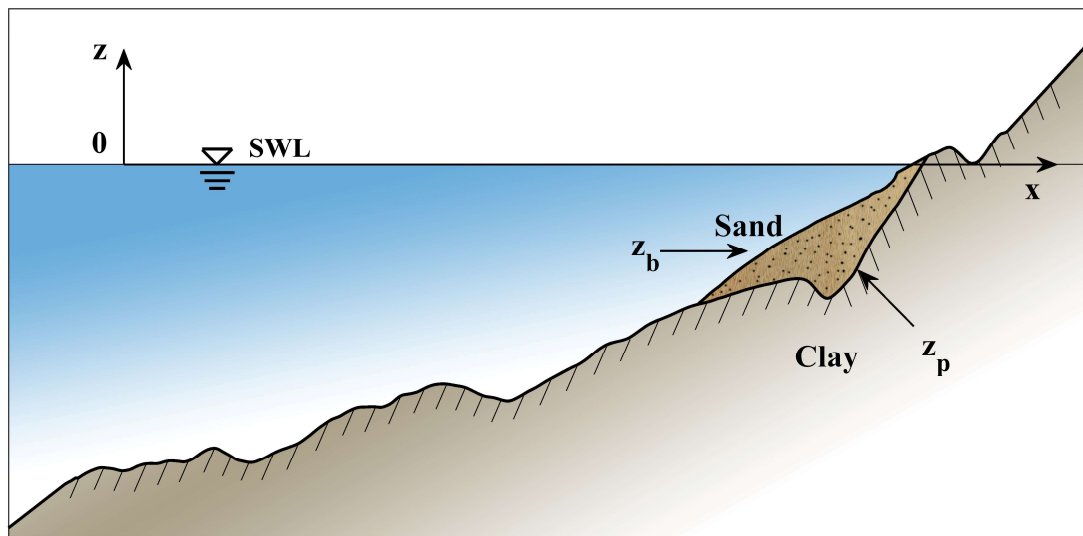


Figure 2.1 Definition sketch for sand surface elevation z_b and clay surface elevation z_p

2.2 Sand Volume Conservation Equation

Sand transport and clay erosion under wave action are formulated as illustrated in Figure 2.1. The cross-shore coordinate x is positive landward with $x = 0$ at the seaward boundary where the spectral significant height H_{m0} and peak period T_p are specified as input to CSHORE. The vertical coordinate z is positive upward with $z = 0$ at the still water level (SWL). Alongshore uniformity and normally incident waves are

assumed. The surface elevations of sand and clay are denoted as z_b and z_p , respectively, in Figure 2.1. The sand layer thickness h_p is given by

$$h_p(t, x) = [z_b(t, x) - z_p(t, x)] \geq 0 \quad (2.1)$$

where t = morphological time for z_b and z_p . The initial profiles $z_b(x)$ and $z_p(x)$ at $t = 0$ are input to CSHORE. The vertical clay erosion depth E is defined as

$$E(t, x) = [z_p(t = 0, x) - z_p(t, x)] \geq 0 \quad (2.2)$$

where $E = 0$ at $t = 0$ and E is positive or zero because of no recovery of eroded clay.

The conservation equation of sand volume per unit horizontal area on the clay surface is expressed as

$$(1 - n_p) \frac{\partial h_p}{\partial t} + \frac{\partial}{\partial x} (q_b + q_s) = f_c \frac{\partial E}{\partial t} \quad (2.3)$$

where n_p = porosity of the deposited sand taken as $n_p = 0.4$; q_b and q_s = cross-shore bed load and suspended load transport rates (no void and positive onshore) per unit width, respectively; and f_c = sand volume per unit volume of cohesive sediment. The sand fraction f_c is in the range of $0 \leq f_c < (1 - n_p)$. For the case of $f_c = (1 - n_p)$, Eq. (2.3) with Eqs. (2.1) and (2.2) can be reduced to the standard continuity equation of bottom sediment. The formulas of q_b and q_s in CSHORE account for limited sand availability and the values of q_b and q_s are proportional to (h_p/d_{50}) with d_{50} = median sand diameter for the case of $h_p < d_{50}$. The right-hand side of Eq. (2.3) expresses the rate of sand volume released from the eroding cohesive sediment. The released sand and the sand in the bedload and suspended load are assumed to be the same.

Eq. (2.3) is expressed in terms of the sand surface elevation z_b to interpret the temporal change of z_b . Substitution of Eqs. (2.1) and (2.2) into Eq. (2.3) yields the equation for sand surface elevation $z_b = (z_s + z_c)$ which is separated into

$$(1 - n_p) \frac{\partial z_s}{\partial t} + \frac{\partial}{\partial x} (q_b + q_s) = 0 \quad (2.4)$$

$$\frac{\partial z_c}{\partial t} = - \left(1 - \frac{f_c}{1 - n_p} \right) \frac{\partial E}{\partial t} \quad (2.5)$$

Eq. (2.4) for z_s is the same as the continuity equation of bottom sediment used in cross-shore sand transport models including CHSORE for the case of fixed bottom ($E = 0$) and expresses the temporal change of z_b caused by the cross-shore sand transport gradient. Eq. (2.5) for z_c gives the additional change of z_b resulting from the cohesive bottom (clay) erosion below the sand layer. The lowering of the sand layer bottom caused by clay erosion is reduced with the increase of the sand volume fraction f_c from zero to $(1 - n_p)$. The fine sediment in the eroded clay is assumed to be suspended and transported seaward of $x = 0$.

2.3 Adjusted Dike Erosion Model

The dike erosion model by Kobayashi and Weitzner (2015) is adjusted to predict the clay erosion depth E

$$\rho R_c \frac{\partial E}{\partial t} = F (e_B D_B + e_f D_f) \quad (2.6)$$

where ρ = fluid density; R_c = dimensional clay resistance parameter; F = dimensionless abrasion and protection function introduced in this study where $F = 1$ for no sand effect on clay erosion; D_B and D_f = energy dissipation rates per unit horizontal area caused by wave breaking and bottom friction, respectively; and e_B and e_f = empirical efficiencies for D_B and D_f , respectively.

The values of R_c , e_B , and e_f in Eq. (2.6) with $F = 1$ were calibrated using large-scale erosion tests of grassed and boulder clay slopes of 1/4 and 1/3 (vertical/horizontal), respectively. The calibrated values were $R_c = 10 \text{ m}^2/\text{s}^2$, $e_B = 0.0002$, $e_f = 0.01$. The

formulas for D_B and D_f in CSHORE include the breaker ratio parameter γ and the wave friction factor f_b . Calibrated values of γ are typically $\gamma = 0.7$ for steep dike slopes and $\gamma = 0.6$ for gentler sandy beaches. Kamphuis (1990) conducted laboratory experiments using glacial till samples from a Lake Erie foreshore and estimated $f_b = 0.0034$ for the till.

CSHORE with Eqs. (2.4) – (2.6) is compared in the next chapter with the till shore erosion data by Bishop et al. (1992), Bishop and Skafel (1992), and Skafel and Bishop (1994). The clay resistance parameter R_c for the till is calibrated starting from $R_c = 10 \text{ m}^2/\text{s}^2$ for the Dutch boulder clay (Wolters et al. 2008). The efficiency e_B is adjusted to $e_B = 0.0002 \times Q$ where Q = fraction of irregular breaking waves computed in CSHORE because Eq. (2.6) with $F = 1$ overpredicted the boulder clay erosion in the outer breaker zone where Q is of the order of 0.1. The adjustment may be regarded to account for the downward decrease of turbulence generated by breaking waves in the outer breaker zone. The roller effect of breaking waves is included in CSHORE for the computation of wave transformation on a beach. The roller effect is negligible on steep slopes because of the limited horizontal distance of roller development (Kobayashi 2016). The dissipation rate D_B in Eq. (2.6) is replaced by the roller energy dissipation rate D_r where D_B is the source of the roller energy.

Eq. (2.6) with $F = 1$ may be acceptable for the case of no or little sand on the clay surface, but $F = 1$ is not realistic for the case of a thick sand layer on the clay surface. The dimensionless function F should increase from unity for a thin mobile layer because of its abrasive effect, whereas F should approach zero for a thick sand layer because of its protective effect. The abrasion and protection function is assumed to depend on the sand layer thickness

$$F = (1 + C_a P_b h_*) \exp(-C_p h_*) ; h_* = h_p/d_{50} \quad (2.7)$$

where h_* = ratio of the sand layer thickness h_p to the median sand diameter d_{50} ; P_b = probability of sand movement computed in CSHORE; C_a = abrasion coefficient; and C_p = protection coefficient.

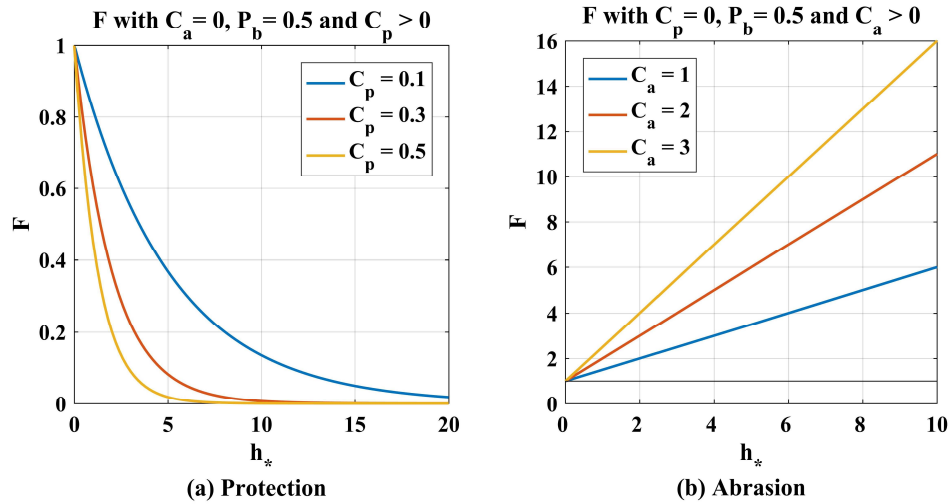


Figure 2.2 Abrasion and protection function as a function of h_* with (a) $C_a = 0, C_p > 0$ and (b) $C_p = 0, C_a > 0$

Eq. (2.7) yields $F = 1$ for the case of $h_p = 0$ (no sand) and for the case of $C_a = 0$ and $C_p = 0$. Figure 2.2(a) for protection only ($C_a = 0$ and $C_p > 0$) shows that F decreases from unity and approaches zero with the increase of h_* from zero. The protective effect increases (decrease of F) as the protection coefficient C_p increases from 0.1 to 0.5 for $P_b = 0.5$. Figure 2.2(b) for abrasive effect only ($C_a > 0$ and $C_p = 0$) indicates that F increases from unity with the increase of h_* from zero. The abrasion

effect increases with the increase of C_a from unity to three for $P_b = 0.5$ (sand movement occurs) in Figure 2.2(b).

Eq. (2.7) appears to be reasonable physically but the empirical coefficients C_a and C_p need to be estimated using available data. These coefficients modify mostly the cross-shore variation of the clay surface erosion rate in Eq. (2.6) and the sand supply rate in Eq. (2.5). The clay resistance parameter R_c affects the magnitude of the clay erosion rate. The breaker ratio parameter γ modifies the cross-shore variation of the hydrodynamic forcing term in Eq. (2.6). Sand transport on the clay surface determines the cross-shore variations of h_p and P_b in Eq. (2.7).

2.4 Computation Procedure

The initial sand profile $z_b(x)$ and clay profile $z_p(x)$ and the cross-shore variations of f_c in Eq. (2.5) and R_c in Eq. (2.6) are specified at time $t = 0$ before the time-marching computation. The initial sand layer thickness $h_p(x)$ is calculated using Eq. (2.1). The clay erosion depth $E(x)$ defined in Eq. (2.2) is zero at $t = 0$. The time series of the still water level, spectral significant wave height H_{mo} and peak period T_p at the seaward boundary $x = 0$ are also specified where wave setdown or setup is neglected at $x = 0$ outside the surf zone.

The computation from given time t to the next time level $(t + \Delta t)$ with $\Delta t =$ time step is outlined in Figure 2.3. The hydrodynamic model in CSHORE is used to compute the breaking wave fraction Q and the dissipation rates D_r and D_f in Eq. (2.6) where D_B is replaced by D_r because a roller is included for wave transformation on a beach. The sand transport model in CSHORE is used to compute the cross-shore bed load and suspended load transport rates q_b and q_s in Eq. (2.4) and sand movement

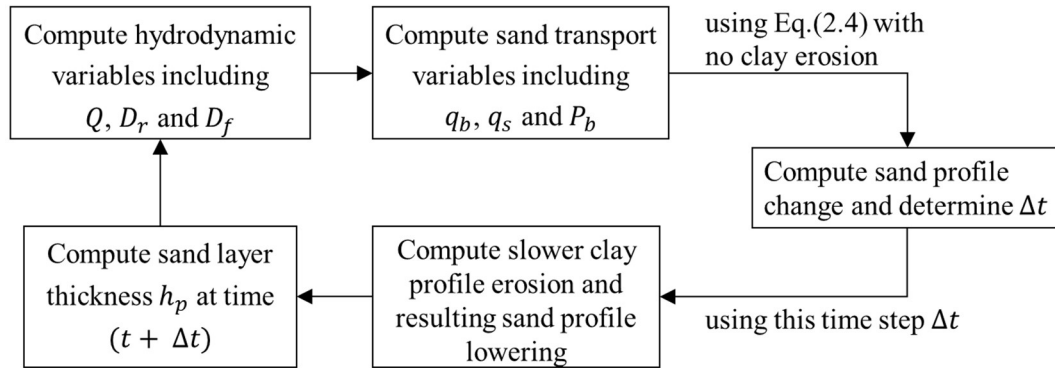


Figure 2.3 Numerical scheme adopted in CSHORE of the computation from the given time t to the next time level $(t + \Delta t)$.

probability P_b in Eq. (2.7). The sand continuity equation given by Eq. (2.4) with no clay erosion is solved using an explicit numerical scheme adopted in CSHORE to obtain the increment Δz_s of $z_s(x)$ for this time step. The time step Δt is computed to satisfy the numerical stability of this explicit scheme. Using this time step Δt , Eqs. (2.5) and (2.6) with Eq. (2.7) are solved to obtain slower clay profile erosion depth $E(x)$ and the increment Δz_c of $z_c(x)$ at the next time level. This simple time stepping is numerically stable because the sand profile change is faster than the clay profile change. The increment Δz_b of the sand profile $z_b(x)$ for this time step is the sum of Δz_s and Δz_c . The new clay profile $z_p(x)$ is obtained using Eq. (2.2). Eq. (2.1) gives the sand layer thickness $h_p(x)$ at the next time level. The time-marching computation is repeated until the end of the specified duration. The model run time is of the order of 10^{-3} of this computation duration. For example, the model run time for clay erosion lasting for 100 h is about 1 minute. The computational efficiency is essential for prediction of slow cohesive bottom erosion for a long duration.

During the time marching computation, the conservation of sand volume in the computation domain from $x = 0$ outside the surf zone to the landward limit $x = x_m$ above the swash zone is ensured at each time step because the computed clay erosion and sand transport rate are found to be sensitive to the sand layer thickness h_p . Integrating Eq. (2.3) with respect to time t from $t = 0$ and with respect to the onshore coordinate x from $x = 0$ to $x = x_m$, the conservation equation of sand volume (no void) per unit width is expressed as

$$A_d(t) = A_t(t) + A_e(t) \quad \text{for } 0 \leq x \leq x_m \quad (2.8)$$

with

$$A_d(t) = (1 - n_p) \int_0^{x_m} [h_p(t, x) - h_p(t = 0, x)] dx \quad (2.9)$$

$$A_t(t) = V_x(t, x = 0) - V_x(t, x = x_m); \quad V_x = \int_0^t (q_b + q_s) dt \quad (2.10)$$

$$A_e(t) = \int_0^{x_m} f_c(x) E(t, x) dx \quad (2.11)$$

where A_d = sand volume per unit width deposited on the clay surface; A_t = cumulative sand volume transported into the computation domain; V_x = cumulative sand volume transported onshore per unit width computed in CSHORE; A_e = sand volume per unit width released from the eroded clay. The following computation is limited to the case of no sand ($h_p = 0$) at $t = 0$ and no sand supply or loss ($V_x = 0$) at $x = x_m$.

Chapter 3

COMPARISON WITH AVAILABLE DATA

This chapter summarizes available hydraulic tests of till erosion in a laboratory flume. The extended model CSHORE is compared with the experiment data. Input parameters for CSHORE are calibrated on the basis of the comparison of the wave hydrodynamics and erosion rate.

3.1 Till Erosion Experiment

Bishop et al. (1992) carried out till excavation to collect intact till samples from a site on the north shore of Lake Erie. 25 till blocks were excavated where each till block was 1.0 m long, 0.35 m wide and 0.45 m high. The till samples consisted of 21% sand and gravel, 33% silt, and 46% clay on average. According to size analysis and geotechnical tests in the report of Bishop and Skafel (1992), the percentage of each sediment corresponded to its mass fraction, but the sediment density was not given. The laboratory experiment was conducted in a 0.37 m wide and 1.4 m high channel built inside a wave flume of 100 m length and 4.5 m width. The initial till profile was constructed as an equilibrium beach profile of sand and confirmed in a preliminary test with available sand. The medium sand diameter d_{50} was 0.51 mm. Eight till blocks were placed between fixed plane slopes where the landward and seaward slopes were approximately 0.19 and 0.13, respectively. An optical profiler was used to measure the vertical profile within the error of about 1 mm. Irregular waves were generated in water

depths of 0.75 – 1.00 m while the significant wave heights (H_{mo}) were in the range of 0.26 – 0.31 m. The spectral peak periods (T_p) varied between 2.6 and 3.0 s. A number of tests were conducted by varying conditions of sand cover and still water level.

Bishop and Skafel (1992, 1994) presented the measured bottom profiles and erosion rates for a sequence of tests. The measured erosion rates were of the order of 0.05 cm/h. The erosion rate increased landward monotonically and peaked in the zone of dominant wave breaking. Thin layers of moving sand were found to increase erosion rates. Conversely, thicker or stationary layers of sand were observed to protect the underlying till. A sand layer of 1 cm or more thickness was sufficient to prevent till erosion. However, the cross-shore variation of the sand layer thickness was not reported perhaps because of the difficulty in measuring the sand layer thickness of the order of 1 mm. The reported bottom profile was truncated below the still water level (SWL) perhaps because of local erosion at the joints and seams between the till blocks near and above the SWL.

Skafel (1995) presented the hydrodynamic data and erosion rate data for two tests. The two tests were named in this report as S75 and S85 with the water depth of 75 and 85 cm. The measured till profiles are showed in Figure 3.1. The reported profiles did not extend to the toe of the profile and to the landward limit of irregular wave runup perhaps because of local erosion and repair at the seams. The seaward and landward plane slopes in Bishop et al. (1992) were added to the measured till profile for the CSHORE computation domain with the onshore coordinate $x = 0$ at the toe of the profile. The waves measured in the water depth of 75 and 85 cm on the horizontal bottom were represented by the significant wave height $H_{mo} = 0.26$ m and peak period $T_p = 3.1$ s as tabulated in Table 3.1. The landward extension was necessary to compute

wave action in the swash zone. Wolters et al. (2008) measured the largest erosion of a clay dike slope of a prototype scale near the still water shoreline.

The extended CSHORE was also compared with two tests in the report by Bishop and Skafel (1992) in light of the uncertain comparison of CSHORE with the S75 and S85 tests. The initial profiles for the two tests named B75 and B85 with the depth of 75 and 85 cm are compared with the profiles of S75 and S85 in Figure 3.2. The initial profile near and above the shoreline was higher for B75 and B85 which may have conducted earlier in the sequence of tests performed by Bishop and Skafel (1992) and Skafel (1995). No hydrodynamic data above the measured bottom profile for the B75 and B85 tests were reported. The spectral significant wave height H_{mo} was 0.26 and 0.25 m for B75 and B85, respectively. The spectral peak period T_p was 2.6 and 3.1 s for B75 and B85, respectively (Table 3.1).

Table 3.1 Spectral significant wave height H_{mo} and spectral peak period T_p for S75, S85, B75, and B85 tests.

Test	Water Depth (cm)	H_{mo} (m)	T_p (s)
S75	75	0.26	3.1
S85	85	0.26	3.1
B75	75	0.26	2.6
B85	85	0.25	3.1

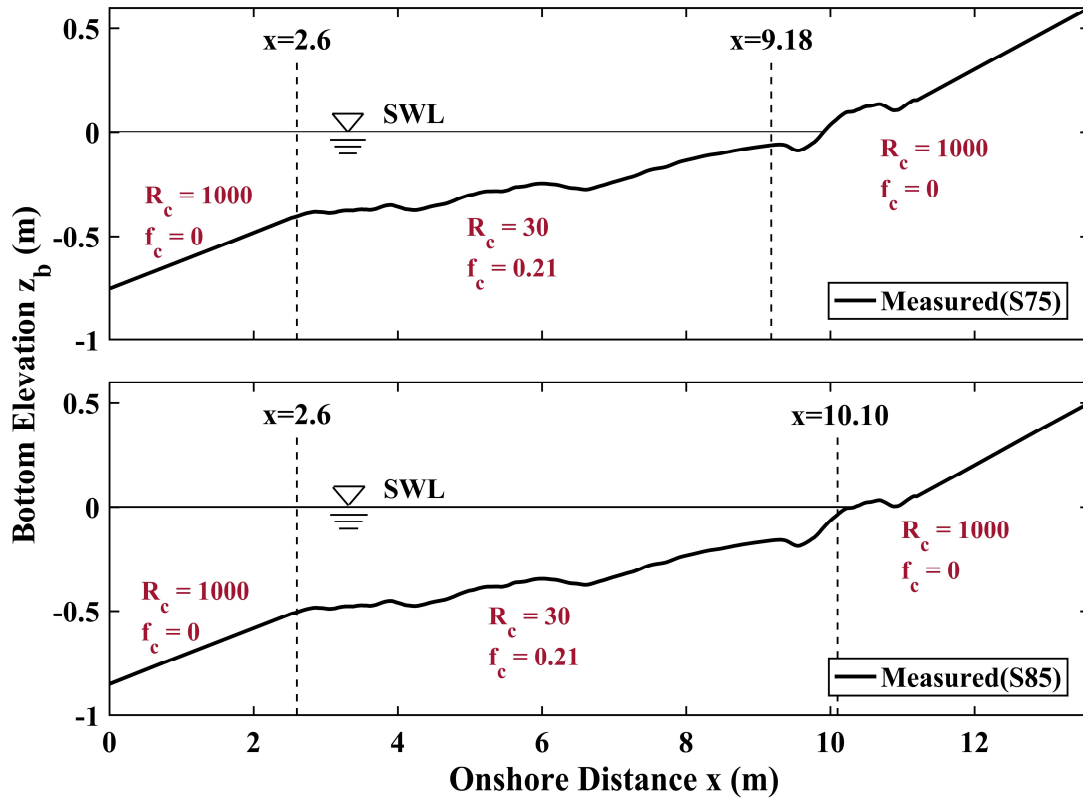


Figure 3.1 Measured initial bottom profiles for S75 and S85 tests with different input values of R_c and f_c

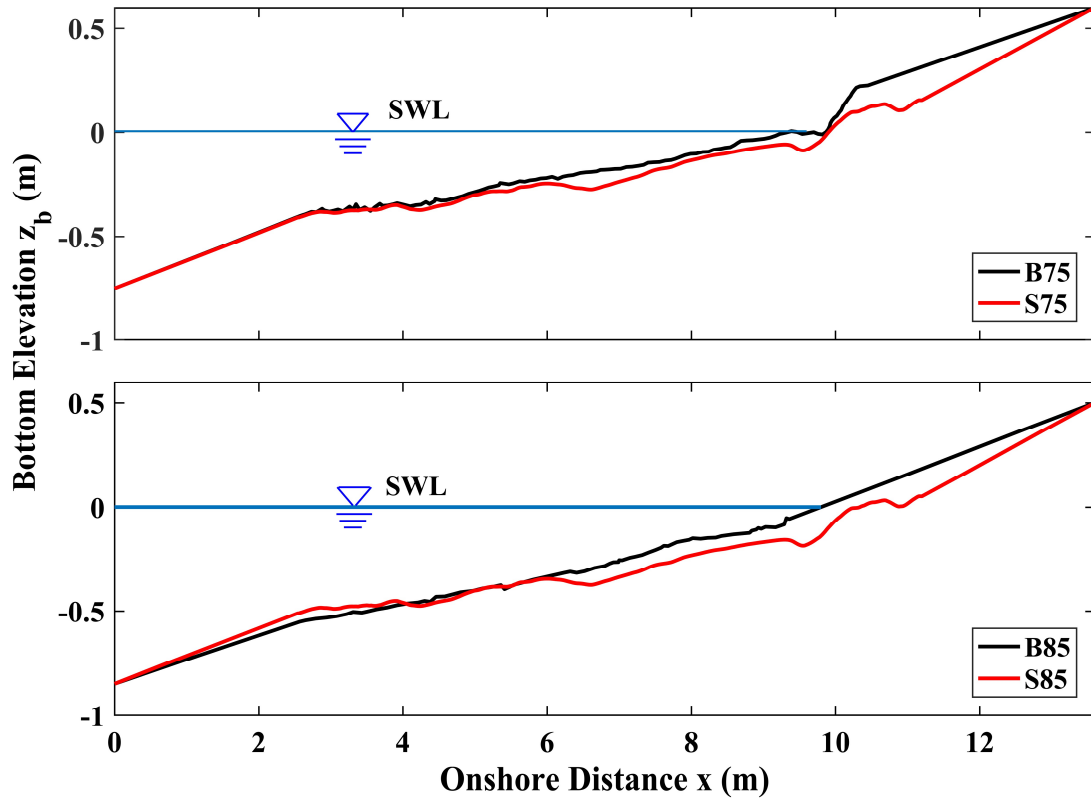


Figure 3.2 Measured initial profiles for B75 and B85 tests in comparison to S75 and S85 profiles

3.2 Initial Profile and Input Parameters

The measured till profiles in Figure 3.1 were assumed to be the initial bottom profiles at $t = 0$ for the S75 and S85 tests. The initial profiles were smoothed over a cross-shore distance of 0.2 m to reduce sudden changes of the bottom slope and possible numerical fluctuations. The initial sand layer thickness $h_p(x)$ at time $t = 0$ was assumed to be zero, which means $z_b(x) = z_p(x)$ at $t = 0$ in Eq. (2.1). The measured till erosion rates of the order of 1mm/h were reported only within the zone of $x = 2.6 - 9.18$ m for S75 test and $x = 2.6 - 10.10$ m for S85 test (Figure 3.1). Figure 3.1 indicates the values of the clay resistance parameter R_c and the sand fraction f_c in the zones with or without the reported erosion rate data. R_c in Eq. (2.6) was calibrated for the S75 and S85 tests and the calibrated value was taken as $R_c = 30 \text{ m}^2/\text{s}^2$. 21% sand and gravel contained in the intact till samples gave the value of $f_c = 0.21$ in Eq. (2.5). In the fixed zones of no erosion data, the values of $R_c = 1000 \text{ m}^2/\text{s}^2$ and $f_c = 0$ were specified as input where $R_c = 1000 \text{ m}^2/\text{s}^2$ corresponded to a grassed dike slope of a prototype scale (Kobayashi and Weitzner 2015).

B75 and B85 tests started from no or little sand on the initial till profile. The reported till profiles for B75 and B85 (Figure 3.2) were extended landward and seaward linearly to match the bottom elevations at $x = 0$ and 13.6 m for the two tests in the same water depth. The cross-shore extent of the till profile was taken as the zone of the till erosion measurement for B75 and B85. The seaward till limit was kept the same as $x = 2.6$ m (Figure 3.1). The landward till limit was $x = 10.02$ m for B75 and $x = 9.37$ m for B85. The values of R_c and f_c in the three zones between $x = 0$ and $x = 13.6$ were the same as those of S75 and S85 tests.

The input parameters for the specific comparisons in this report are listed in Table 3.2. The sediment transport model in CSHORE is limited to a single sediment.

The median sand diameter d_{50} of 0.51 mm and fall velocity of 7.3 cm/s were used for sand transport on the eroding till. The breaker ratio parameter γ is taken as 0.6 or 0.7 to assess hydrodynamic effect on the erosion rate. The abrasion and protection function F given by Eq. (2.7) is plotted as a function of the normalized sand layer thickness $h_* = (h_p/d_{50})$ in Figure 3.3 for $C_a = 2$, $C_p = 0.5$, and $P_b = 0.1, 0.5$, and 1. $F = 1$ at $h_* = 0$ and F is essentially zero at $h_* = 20$ in Eq. (2.7), corresponding to $h_p = 1.0$ cm for $d_{50} = 0.51$ mm. The protection coefficient $C_p = 0.5$ was based on the prevention of till erosion by the sand layer of 1.0 cm thickness described by Skafel and Bishop (1994). The value of the abrasion coefficient $C_a = 2$ was selected to increase the till erosion rate by a thin layer of moving sand, where the probability P_b of sand movement was used to represent the degree of sand movement. These values of the protection and abrasion coefficients should be regarded to be tentative because the sand layer thickness and sand movement were not measured in these tests.

Table 3.2 Input parameters to CSHORE for S75, S85, B75, and B85 tests.

Parameters	Value	Description
Δx	0.02 m	cross-shore nodal spacing
γ	0.6 or 0.7	breaker ratio parameter
d_{50}	0.51 mm	median sand diameter
ω_f	7.3 cm/s	fall velocity
e_B	0.0002Q	breaking wave efficiency for dike erosion
e_f	0.01	bottom friction efficiency for dike erosion
f_b	0.0034	wave friction factor
C_a	2	abrasive efficiency
C_p	0.5	protective efficiency

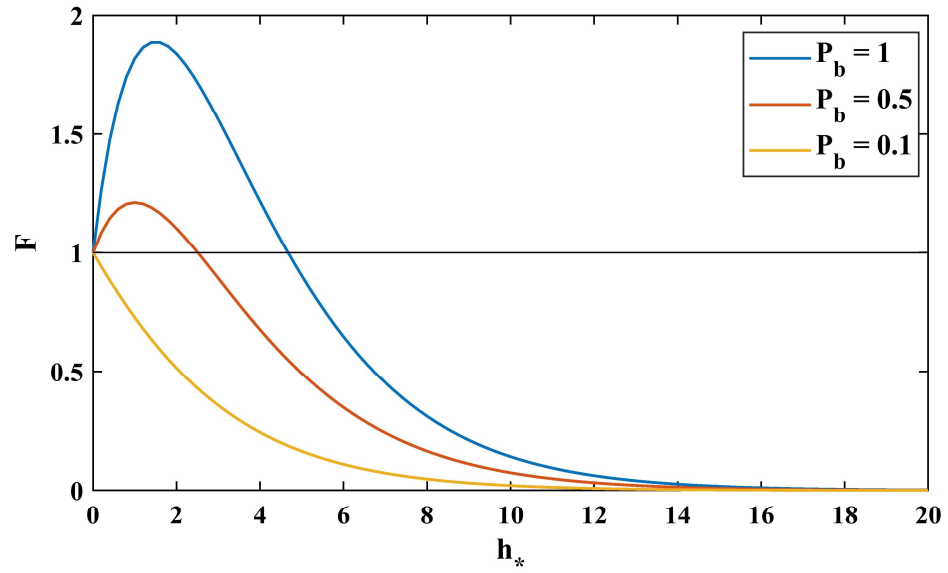


Figure 3.2 Abrasion and protection function F with $C_a = 2$ and $C_p = 0.5$ as a function of normalized sand layer thickness h_*

3.3 Wave Hydrodynamics

The measured hydrodynamic variables for the S75 and S85 tests (Skafel 1995) are compared with the computed results at time $t = 1$ and 10 h for the computation duration of 10 h. The test duration was not stated perhaps because the profile changes were small. The cross-shore variations of the significant wave height H_{m0} , fraction Q of broken waves, and the velocity standard deviation σ_u were reported for the S75 and S85 tests. Figures 3.4 – 3.9 examine the influence of the breaker ratio parameter $\gamma = 0.6$ and 0.7 at $t = 1$ h as well as the difference of the computed results at $t = 1$ and 10 h for $\gamma = 0.6$.

Figures 3.4, 3.6 and 3.8 indicate the influence of γ . The increase of γ delays wave breaking and wave height decay, resulting in the increase of the cross-shore velocity. The measured value of Q was obtained by counting the number of broken and unbroken waves at the given location but the criteria of broken and unbroken waves were not stated. The computed Q seaward of the shoreline was affected by the bottom undulations in Figure 3.1. The velocity was measured at 4 cm above the till surface, whereas the standard deviation of the depth-averaged velocity was computed by CSHORE. This difference may partially explain the overprediction of σ_u .

The differences in the wave hydrodynamics at $t = 1$ and 10 h are shown in Figures 3.5, 3.7 and 3.9. The computed time-averaged hydrodynamic variables changed very little during $t = 1 - 10$ h because the computed profile changes were small. The computed variables related to clay erosion are affected by the small profile changes.

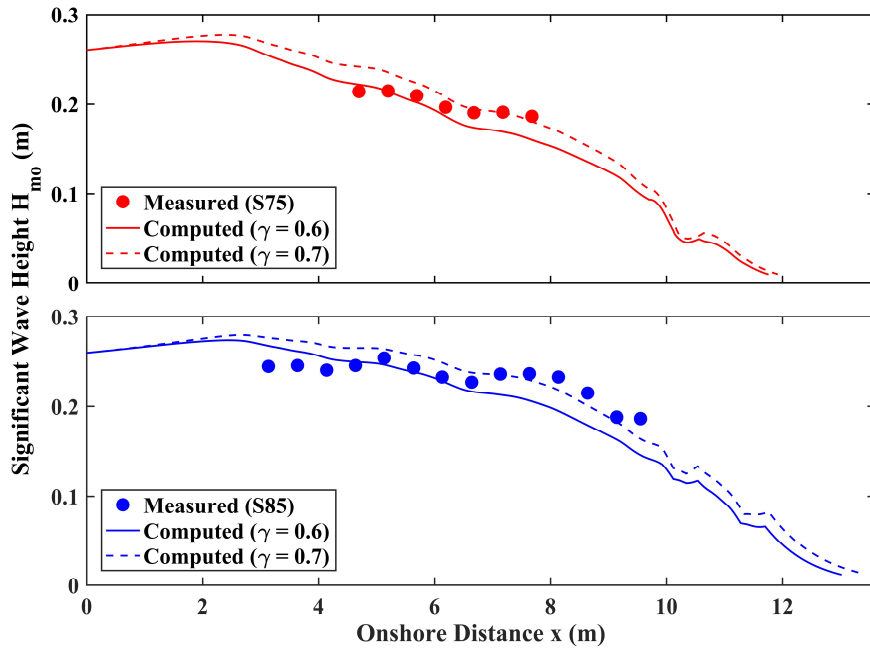


Figure 3.4 Measured and computed ($\gamma = 0.6$ and 0.7 , $t = 1$ h) significant wave height H_{mo} for S75 and S85 tests

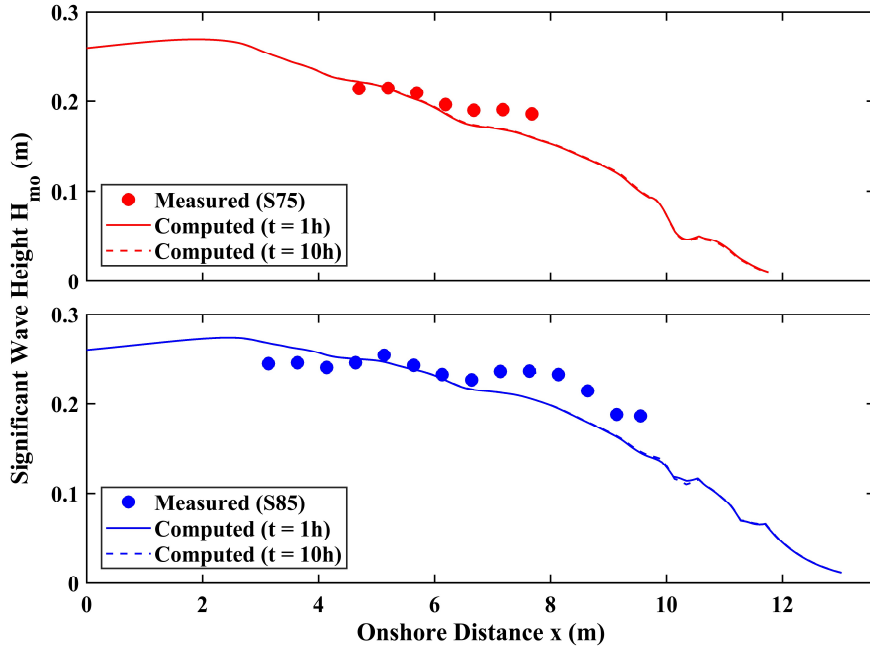


Figure 3.5 Measured and computed ($t = 1$ h and 10 h, $\gamma = 0.6$) significant wave height H_{mo} for S75 and S85 tests

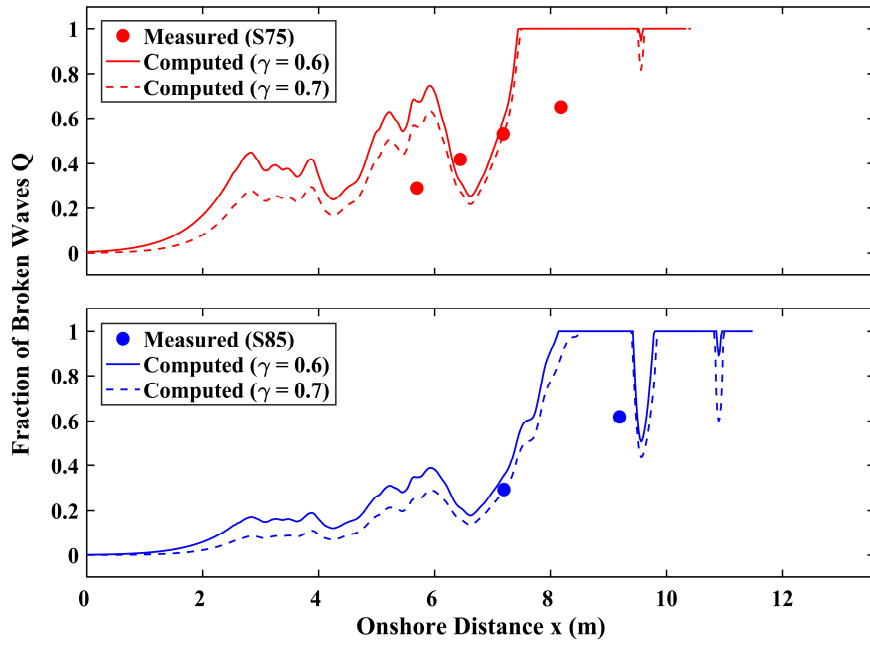


Figure 3.6 Measured and computed ($\gamma = 0.6$ and 0.7 , $t = 1$ h) fraction Q of broken waves for S75 and S85 tests

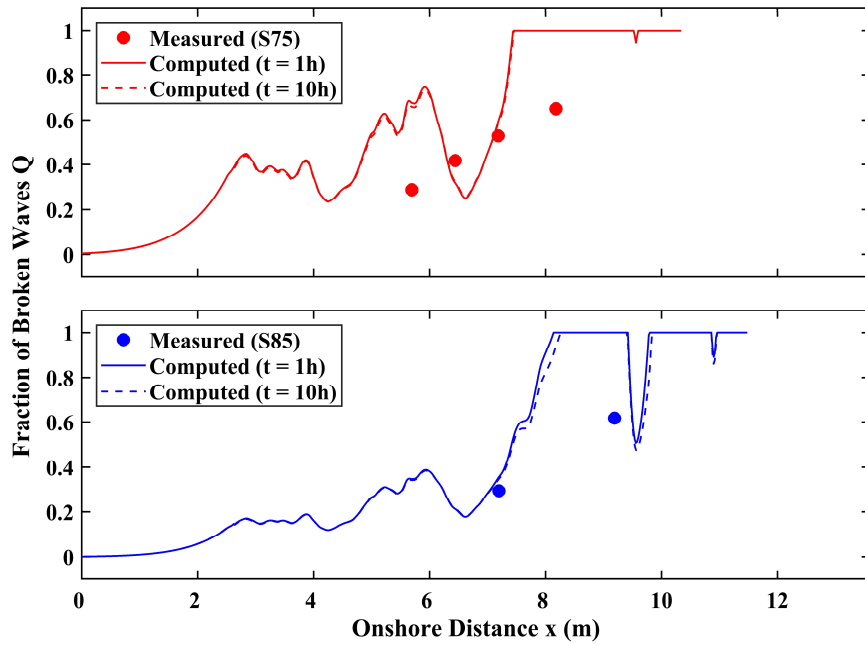


Figure 3.7 Measured and computed ($t = 1$ h and 10 h, $\gamma = 0.6$) fraction Q of broken waves for S75 and S85 tests

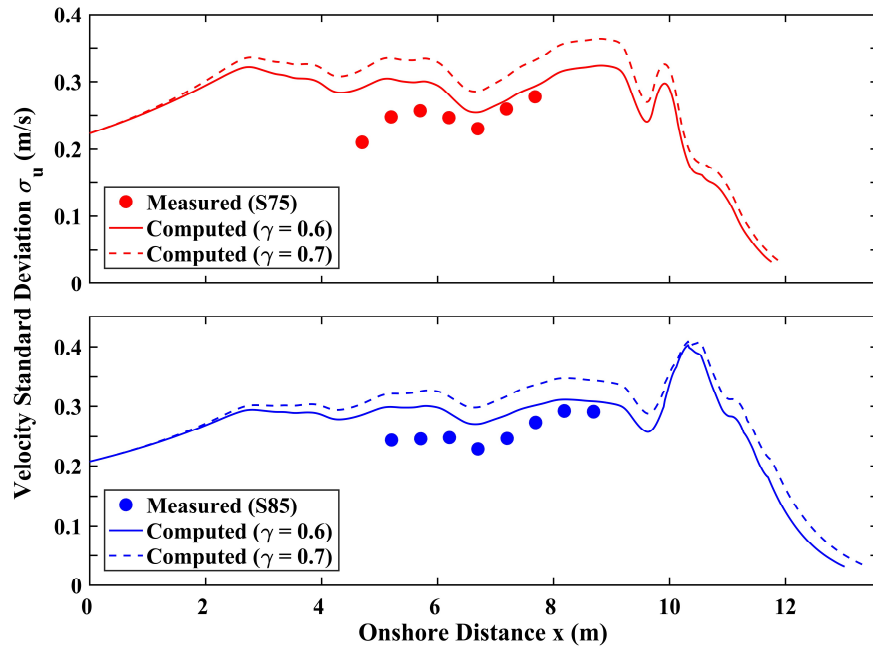


Figure 3.8 Measured and computed ($\gamma = 0.6$ and 0.7 , $t = 1$ h) velocity standard deviation σ_u for S75 and S85 tests

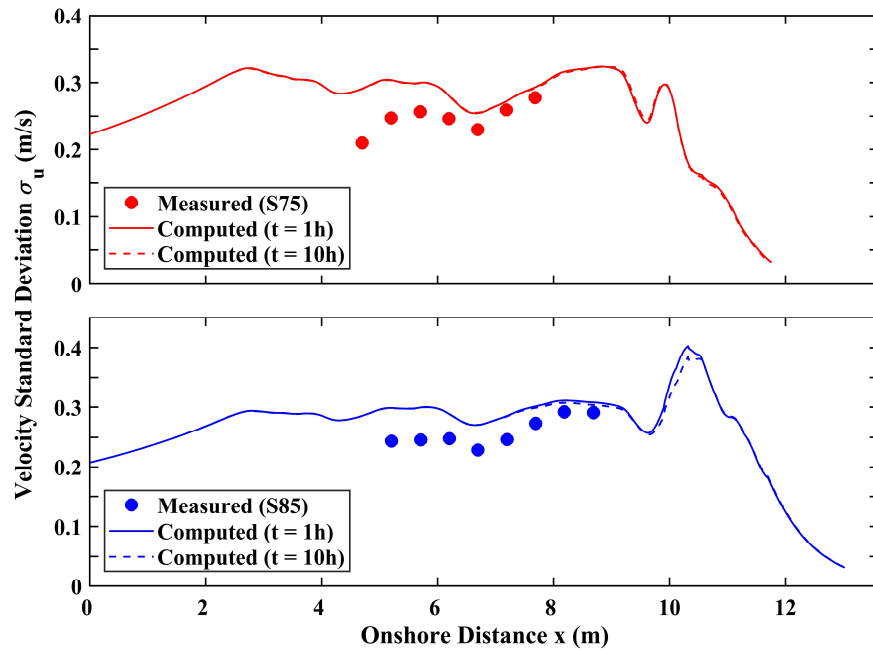


Figure 3.9 Measured and computed ($t = 1$ h and 10 h, $\gamma = 0.6$) velocity standard deviation σ_u for S75 and S85 tests

3.4 Till Erosion Rates

The dike erosion model was adjusted to predict the clay erosion depth E as discussed in Section 2.3. Figures 3.10 and 3.11 compare the measured and computed till erosion rates for the S75 test together with the computed P_b , h_p and F at time $t = 1$ and 10 h with $\gamma = 0.6$ and 0.7, respectively. The measured erosion rate is the smoothed and truncated rate reported by Skafel (1995) who did not specify the test duration. The computed rate is the computed clay erosion depth E divided by time t . The sand movement probability P_b is about 0.2 – 0.3 and is nearly independent of time t . The sand layer thickness h_p is zero at $t = 0$ and increase with time. Sand released from the eroded clay accumulates more near the shoreline. The abrasion and protection function F is unity at $t = 0$. The sand accumulation reduces the value of F and the clay erosion rate. The values of P_b and h_p for $\gamma = 0.7$ are larger than those of $\gamma = 0.6$ because of the increased breaking wave action and clay erosion near the shoreline. The computed erosion rate decreases with time but is almost zero in the fixed bottom zone of $R_c = 1,000 \text{ m}^2/\text{s}^2$.

The measured and computed till erosion rates for the S85 test are compared in Figures 3.12 and 3.13. The water level increase of 10 cm shifts wave breaking and energy dissipation landward. The sand movement probability P_b is increased to around 0.4. The sand layer thickness near the shoreline is larger than 0.5 cm and the function F is reduced to almost zero. The erosion rate (erosion depth E divided by t) decreases from $t = 1$ h to 10 h because this rate decreases with sand accumulation on the eroded clay. The computed erosion rate increases as the breaker ratio parameter γ increases. The measured erosion rate is closer to the computed rate at $t = 10$ h for the S75 and S85 tests. The difference between $\gamma = 0.6$ and 0.7 may be within the uncertainty of the reported erosion rates in these tests.

Figure 3.14 and 3.15 compare the measured and computed till erosion rates for B75 and B85 with $\gamma = 0.6$ and 0.7 , respectively. The measured values were noisy and smoothed over a cross-shore distance of 0.5 m. The comparison of the erosion rates in Figures 3.10 – 3.15 indicates the effect of the initial profile difference. The cross-shore variations of P_b , h_p , and F are similar for the B and S tests. The clay erosion process does not cease at $t = 10$ h in the cases of $\gamma = 0.6$ and 0.7 until sand released from the eroded clay bottom forms a thick sand layer. The measured and computed erosion rates for B75 and B85 are of the same order magnitude. The overall agreement for the clay erosion rates in Figures 3.10 – 3.15 is similar for $\gamma = 0.6$ and 0.7 . The disagreement is hence caused by the shortcomings of the sand transport model and clay erosion model in CSHORE along with the uncertainties of the laboratory data.

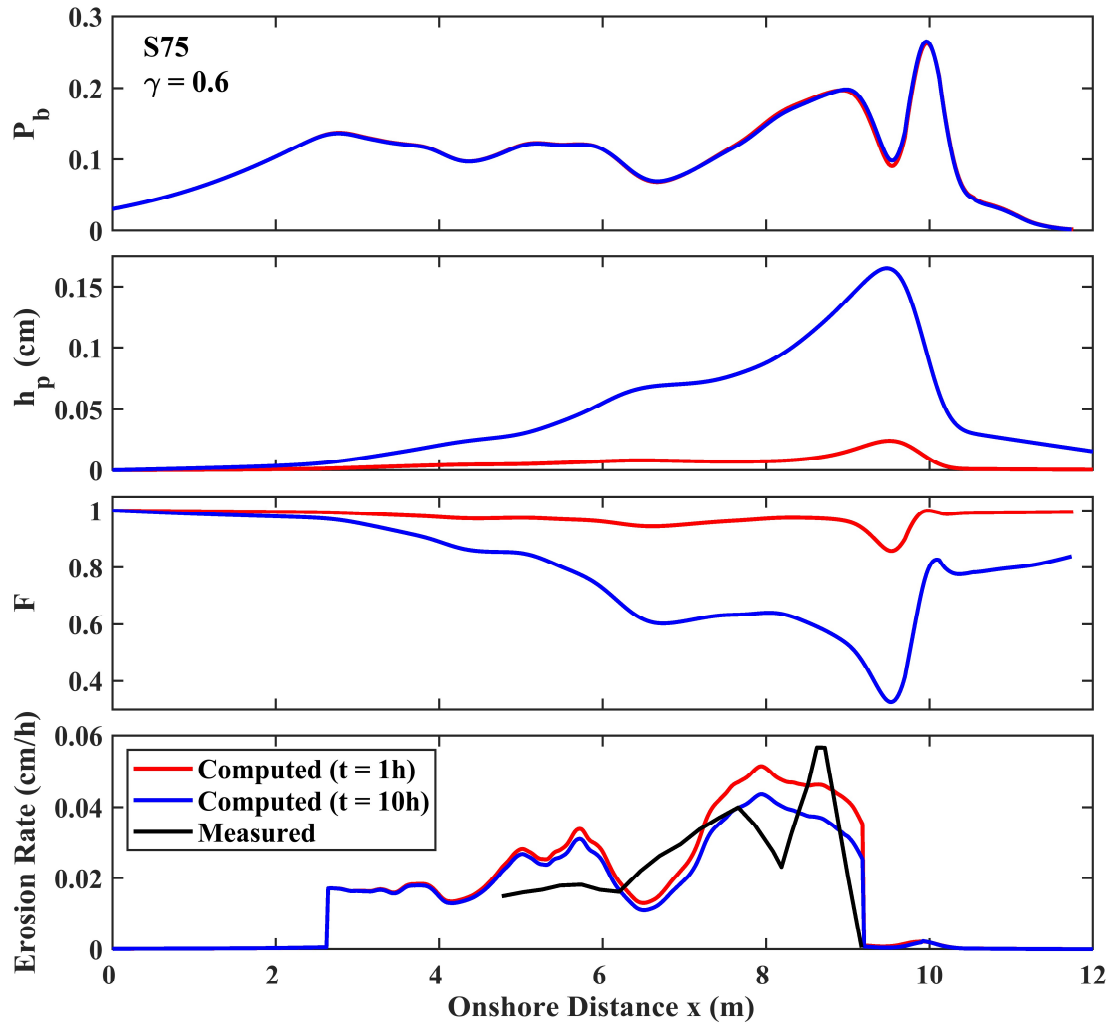


Figure 3.10 Computed ($t = 1$ h and 10 h, $\gamma = 0.6$) sand movement probability P_b , sand layer thickness h_p and abrasion and protection function F as well as measured and computed erosion rates for S75 test.

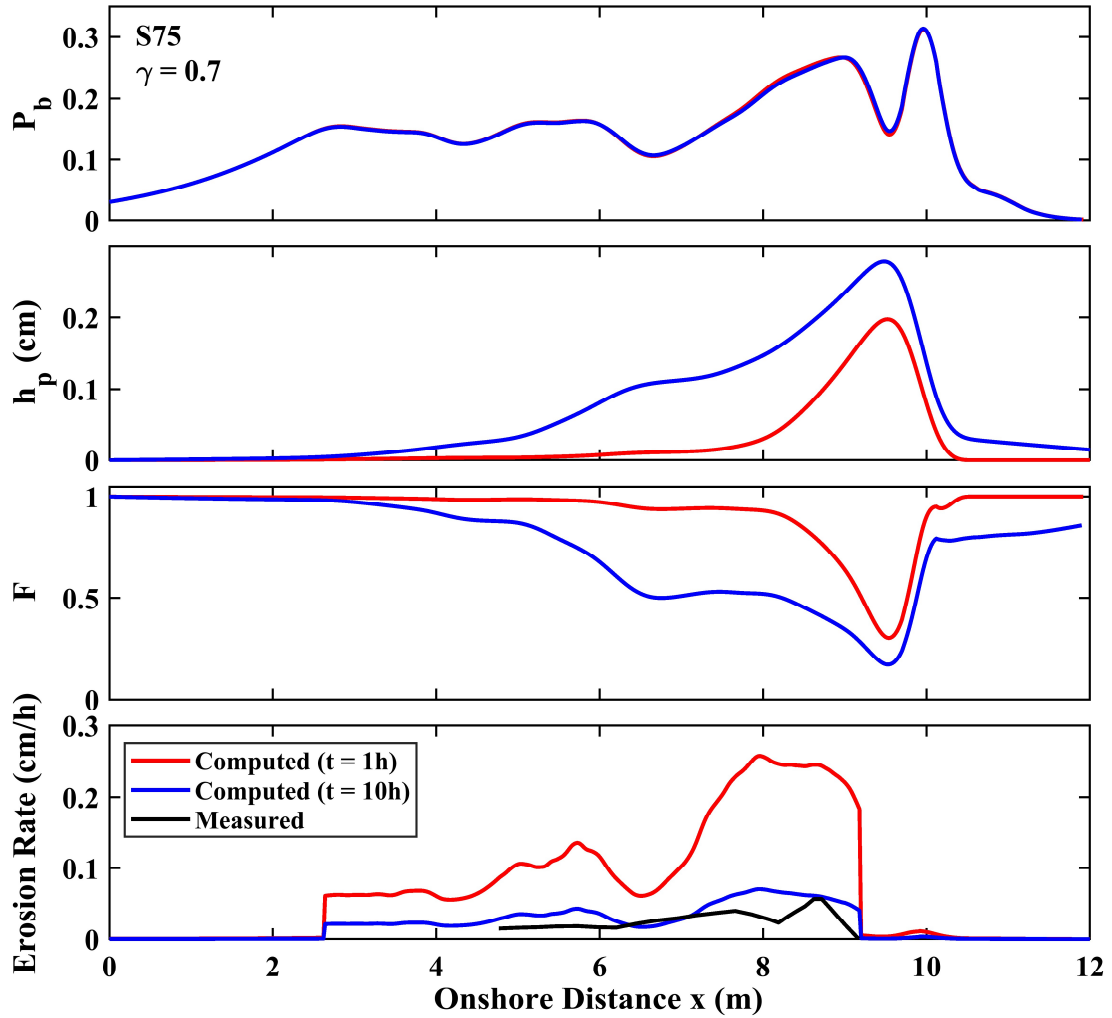


Figure 3.11 Computed ($t = 1$ h and 10 h, $\gamma = 0.7$) P_b , h_p and F as well as measured and computed erosion rates for S75 test.

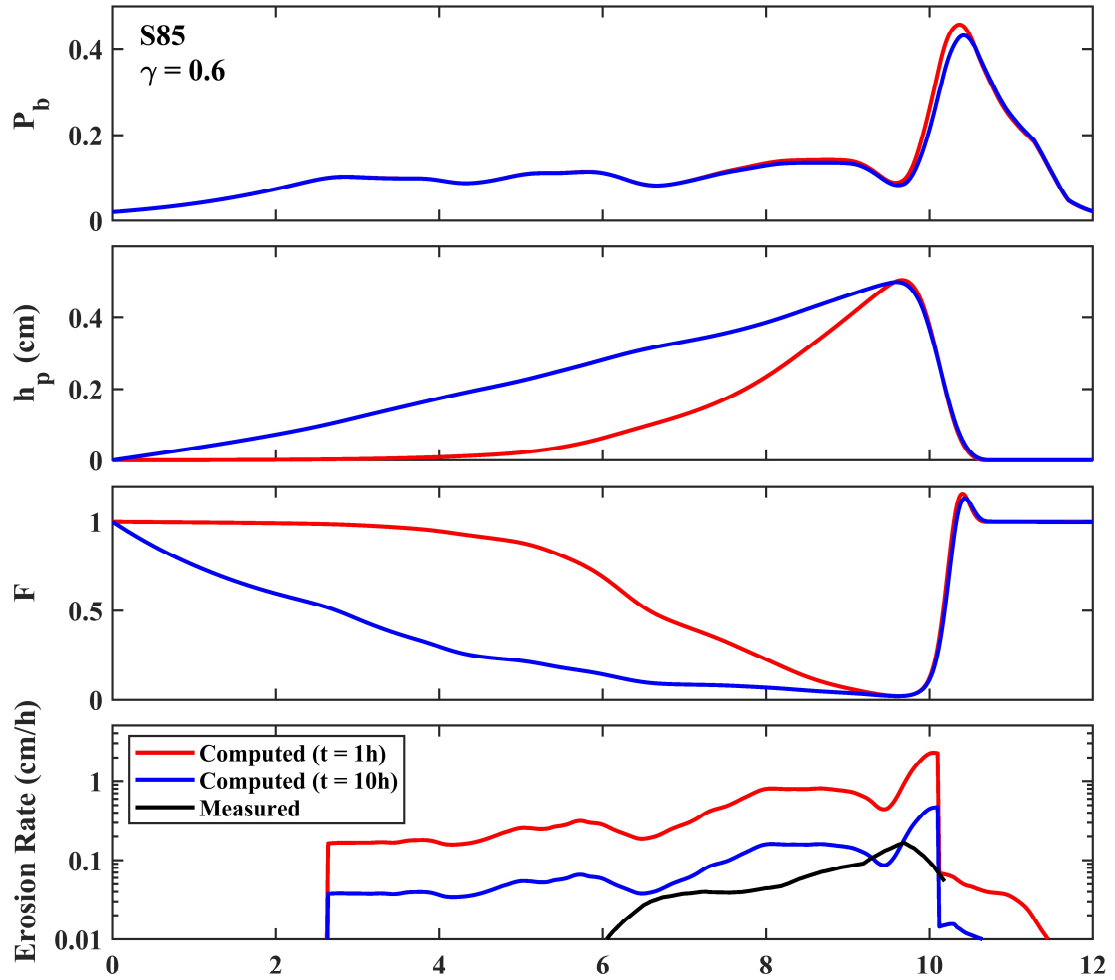


Figure 3.12 Computed ($t = 1$ h and 10 h, $\gamma = 0.6$) P_b , h_p and F as well as measured and computed erosion rates for S85 test.

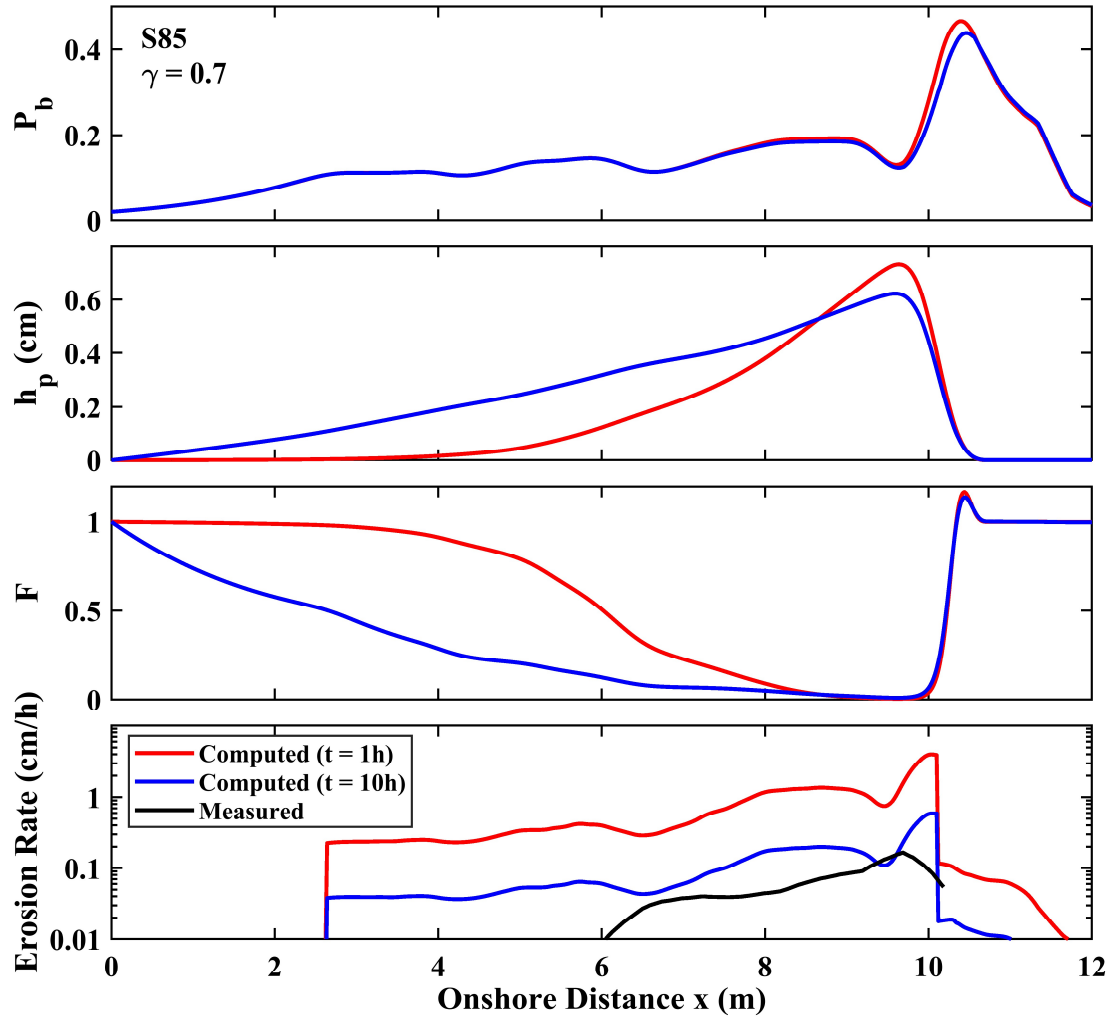


Figure 3.13 Computed ($t = 1$ h and 10 h, $\gamma = 0.7$) P_b , h_p and F as well as measured and computed erosion rates for S85 test.

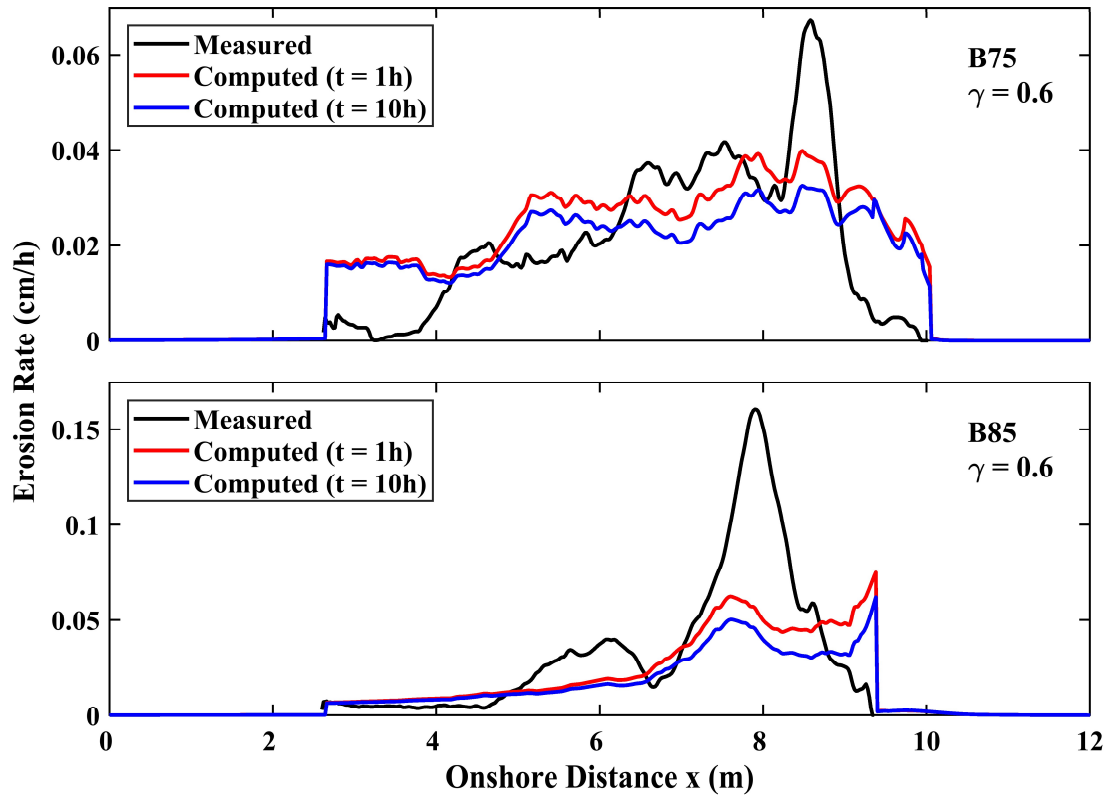


Figure 3.14 Measured and computed ($t = 1$ h and 10 h, $\gamma = 0.6$) erosion rates for B75 and B85 tests.

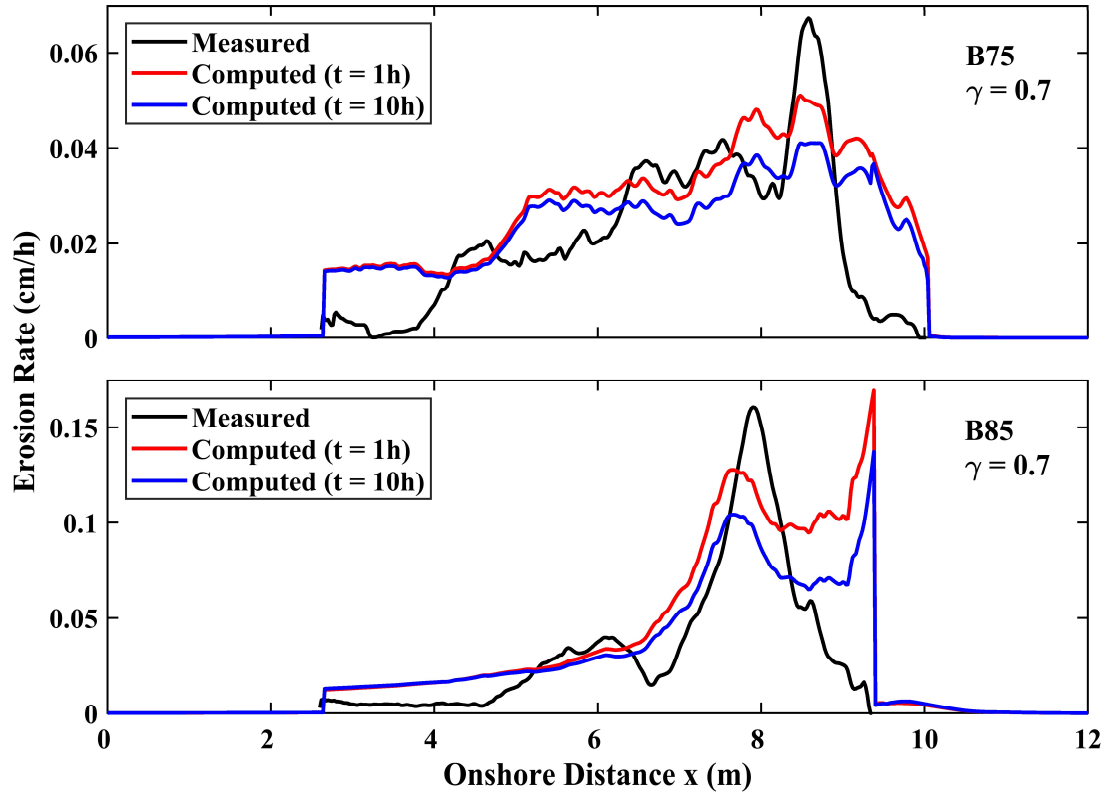


Figure 3.15 Measured and computed ($t = 1$ h and 10 h, $\gamma = 0.7$) erosion rates for B75 and B85 tests.

Chapter 4

APPLICATIONS OF NUMERICAL MODEL

The extended CSHORE may incorporate the fundamental processes of sand and clay interactions for the duration of 10 h, but the local clay erosion less than about 1 cm during 10 h is insignificant for practical applications. Two tests based on the S75 and S85 tests are computed for the duration to 100 h. Another two tests with the duration up to 200 h are computed as the prototype tests. The numerical model CSHORE is applied to simulate the till profile evolution in these hypothetical four tests.

4.1 Longer-Term Model Tests

The computation duration for the S75 and S85 tests is increased to 100 h where the water level and wave conditions are not changed. The initial profile is also kept the same as that in Figure 3.1, but the entire profile from $x = 0 - 13.6$ m is composed of the till with $R_c = 30 \text{ m}^2/\text{s}^2$, $f_c = 0.21$, and $d_{50} = 0.51$ mm. The fixed slopes at the seaward and landward edges are artificial and affect long-term profile evolutions. No sand is present on the initial till profile and thus $z_b(x) = z_p(x)$ at $t = 0$ in Eq. (2.1) remains the same. The typical value of the breaker ratio parameter $\gamma = 0.6$ for beaches is used in the following figures because the profile evolution and erosion rates between $\gamma = 0.6$ and $\gamma = 0.7$ in the longer-term computations are found to be similar. The input parameters listed in Table 3.2 are kept the same.

Figure 4.1 shows the computed cross-shore variations of the sand surface elevation z_b and clay surface elevation z_p at time $t = 0$ and 100 h between the zone of

$x = 4 - 11.5$ m of discernible profile changes for the S75 and S85 tests. The initial profiles of z_b and z_p are the same. The profile evolution is noticeable near the shoreline in the swash zone. However, the sand layer thickness h_p defined as the vertical distance between z_b and z_p in Eq. (2.1) is less than 0.5 cm at $t = 100$ h (Figure 4.2). The sand layer thickness is affected by the sand volume released from the eroded clay and the cross-shore sand transport rate. The computed cross-shore variations of the till erosion rate at time $t = 10, 50,$ and 100 h for the S75 and S85 tests are shown in Figure 4.3. The measured erosion rates in Figures 3.10 – 3.13 are added in Figure 4.3 for comparison. The computed erosion rate, which is the erosion depth E divided by the time t , decreases with time as more sand is released from the eroded till. The maximum erosion depth is less than 6 cm at $t = 100$ h. Clay erosion underneath the deposited sand of limited mobility ceases when the sand layer thickness increases to about 1 cm for this till with $R_c = 30 \text{ m}^2/\text{s}^2$, $f_c = 0.21$, $d_{50} = 0.51$ mm, and sand porosity of 0.4.

The computed cross-shore bedload transport volume v_{bx} , suspended load transport volume v_{sx} , and net sand transport volume $v_x = (v_{bx} + v_{sx})$ per unit width (m^3/m) at time $t = 10, 50,$ and 100 h for the S75 and S85 are shown in Figures 4.4 and 4.5. The cumulative volumes per unit width were used to interpret the net sand transport pattern on a natural beach [e.g., Kobayashi and Zhu 2017]. Sand released from the underlying cohesive bottom is moving onshore or offshore by wave action. The cross-shore bedload transport is positive (onshore) except near the shoreline in the S75 test. The cross-shore suspended load transport is negative (offshore) with the maximum offshore transport near the shoreline. The computed net cross-shore transport is positive in the offshore and surf zones of dominant bedload and negative near the shoreline dominated by suspended sand transported offshore by return current induced by

breaking waves. The magnitude of the net cross-shore transport volume is of the order of 1 (m³/m) at time $t = 100$ h for the S75 and S85 tests. The budget of sand volumes (no void) based on Eqs. (2.8) – (2.11) is presented in Table 4.1. The deposited (A_d) and released (A_e) sand volumes are almost the same and the transported (A_t) sand volume at $x = 0$ is negligible for the S75 and S85 tests. As a result, sand released from the eroded clay is transported and deposited in the vicinity of the shoreline (Figure 4.1)

Table 4.1 Deposited sand volume A_d , transported sand volume A_t , and sand volume A_e released by eroded till for duration of 100 h (Model) or 200 h (Prototype)

Test	Duration (h)	Sand Volume per Unit Width (m ³ /m)		
		A_d	A_t	A_e
S75	100	0.0184	0.00007	0.0184
S85	100	0.0229	0.00004	0.0229
S75P	200	3.29	2.03	1.26
S85P	200	4.76	2.15	2.61

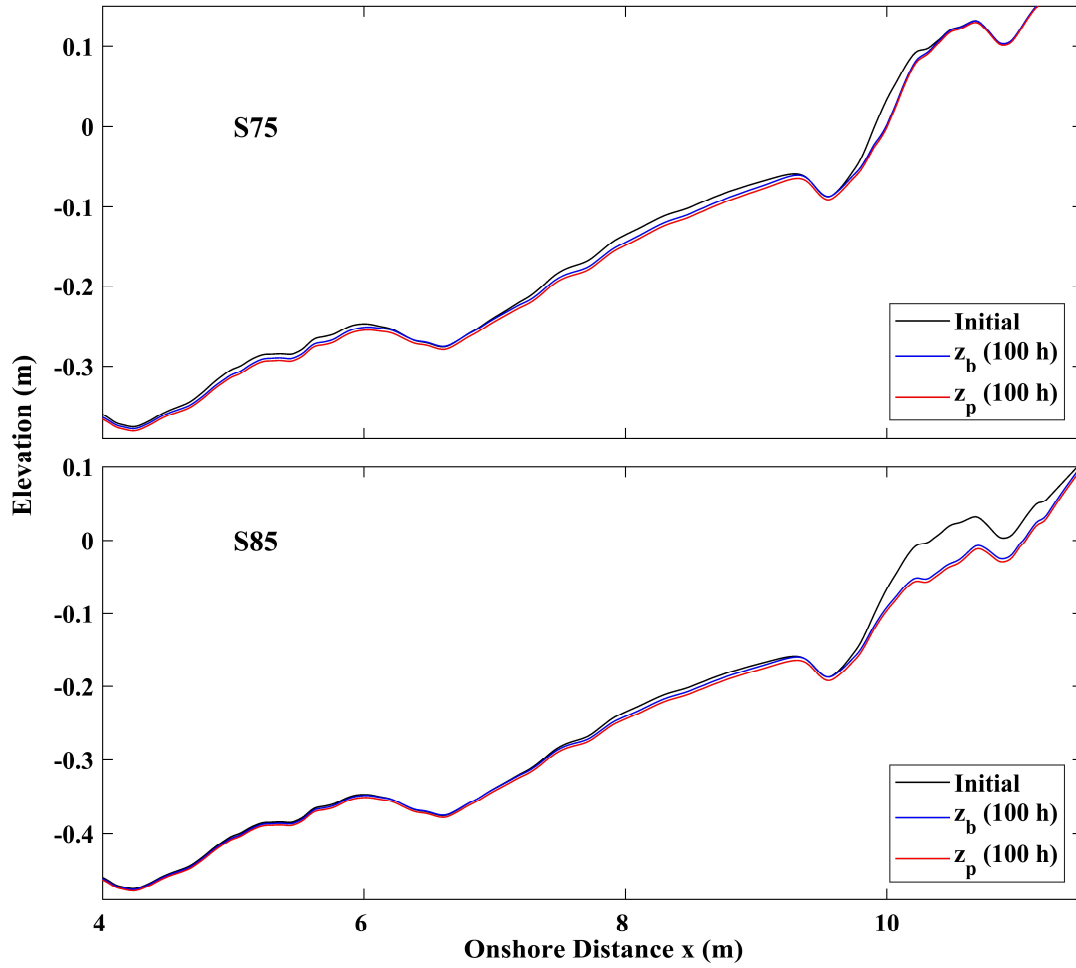


Figure 4.1 Sand surface elevation z_b and clay surface elevation z_p at $t = 0$ and 100 h for S75 and S85 tests

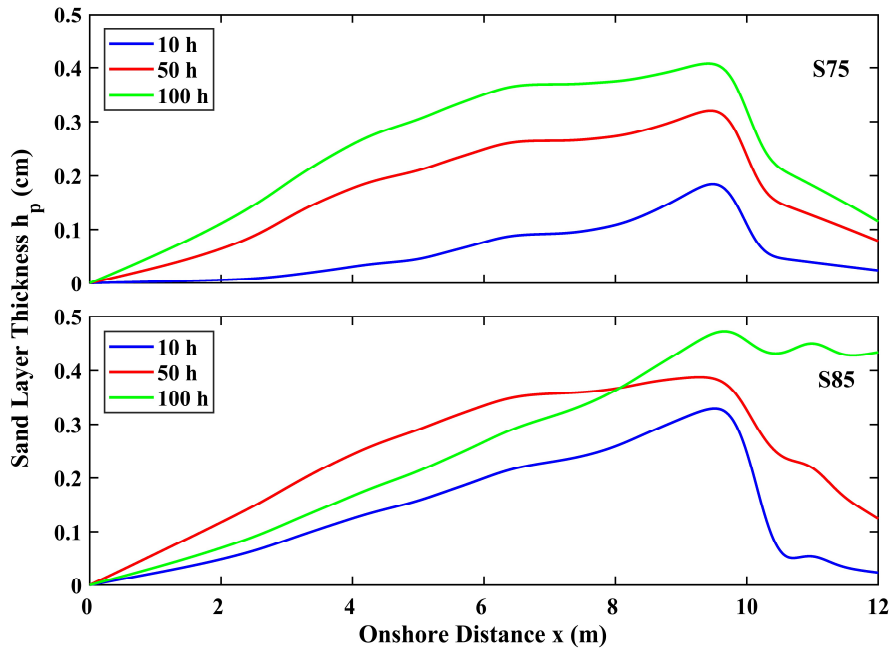


Figure 4.2 Computed sand layer thickness h_p at $t = 10, 50,$ and 100 h for S75 and S85 tests

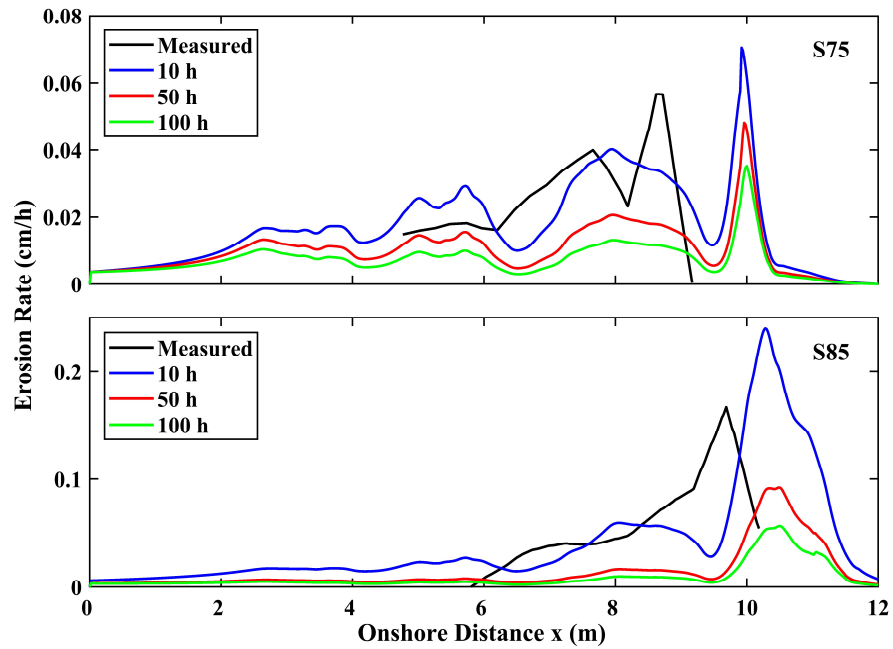


Figure 4.3 Computed erosion rates at $t = 10, 50,$ and 100 h in comparison with measured erosion rate for S75 and S85 tests

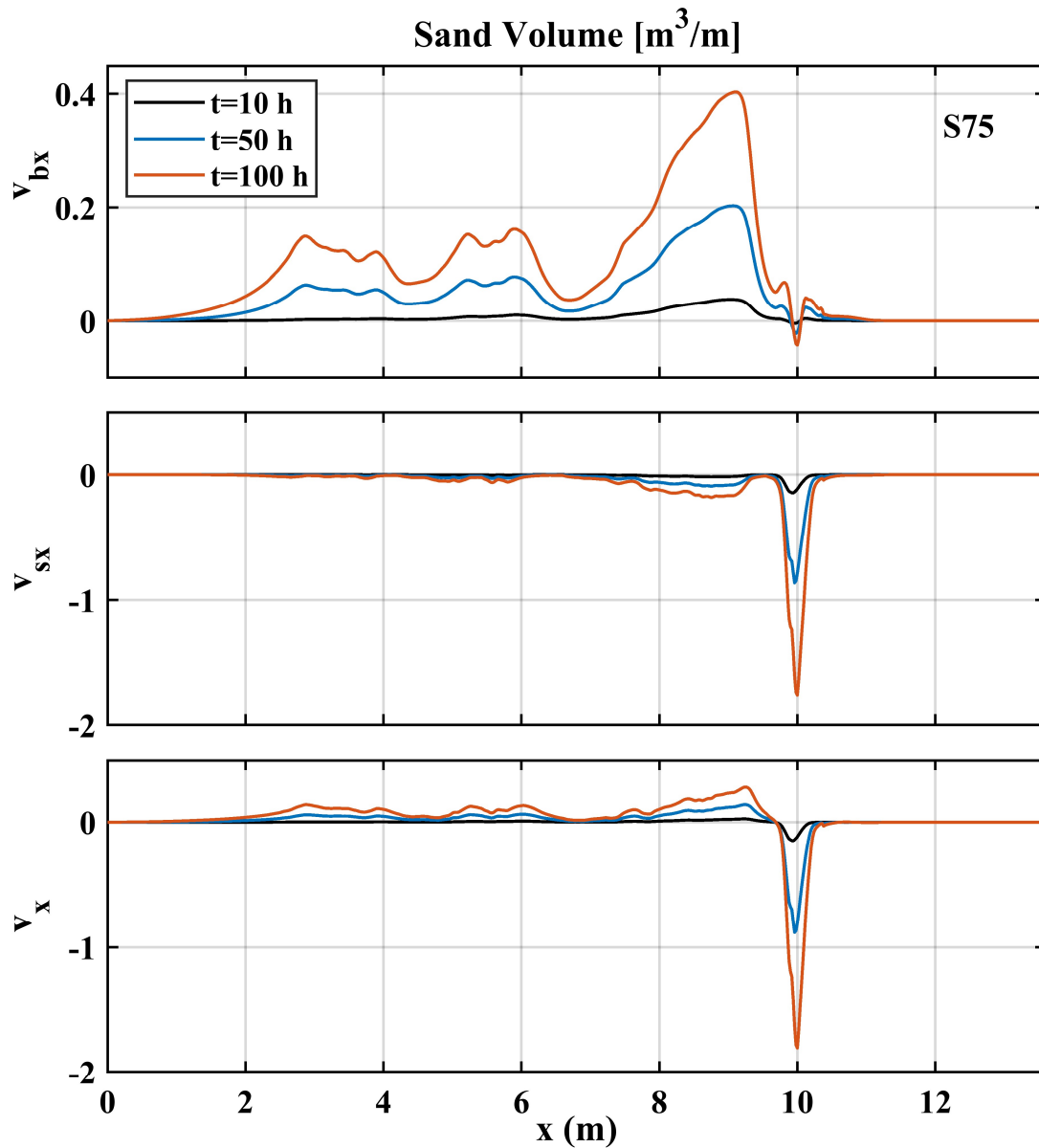


Figure 4.4 Cross-shore bedload transport volume v_{bx} , suspended load transport volume v_{sx} , and net sand transport volume v_x (m³/m) at $t = 10, 50,$ and 100 h for S75 test

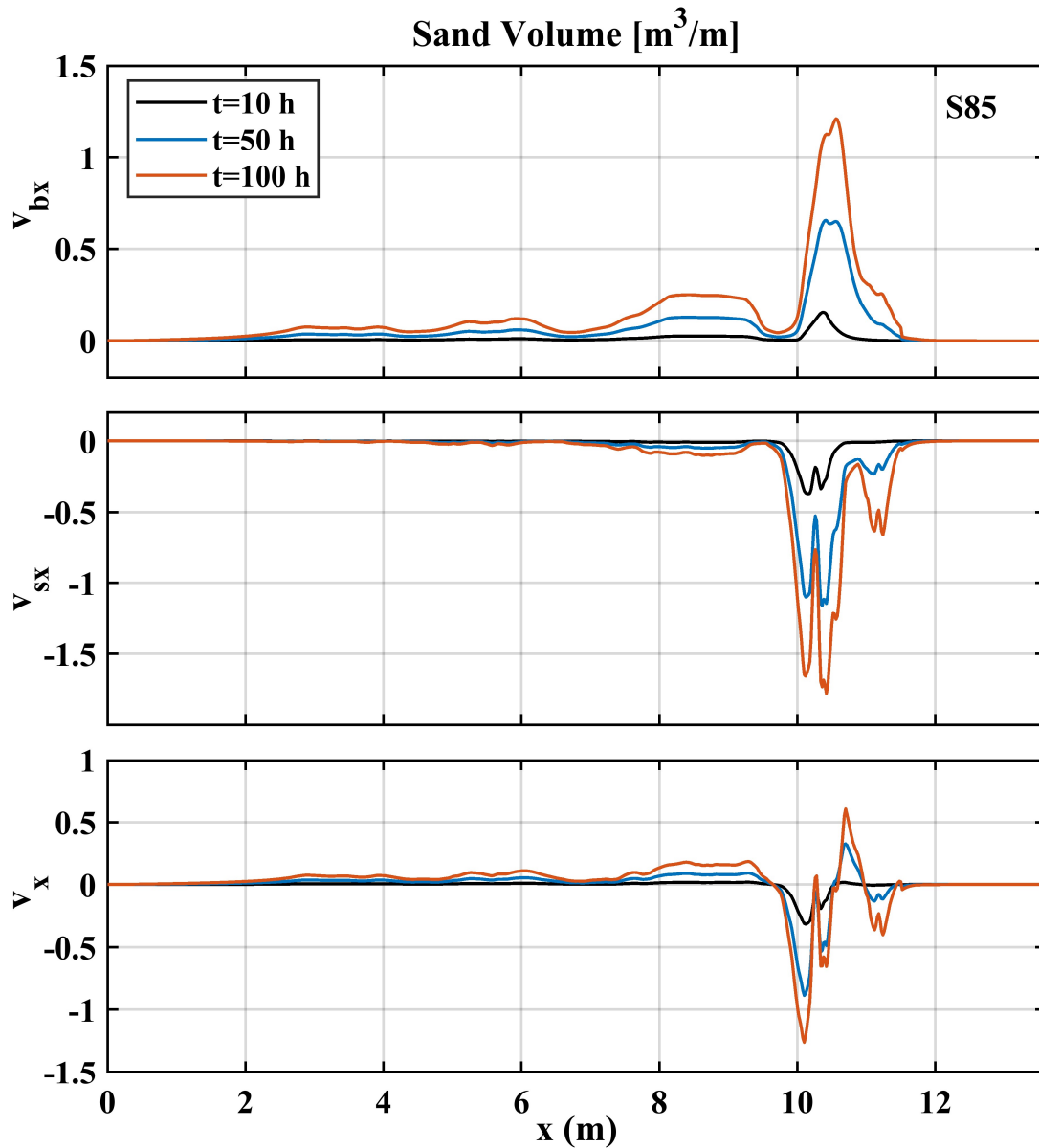


Figure 4.5 Cross-shore sand transport volume v_{bx} , v_{sx} , and v_x (m³/m) at $t = 10, 50,$ and 100 h for S85 test

4.2 Hypothetical Prototype Tests

Hypothetical prototype tests named S75P and S85P are devised to examine the scale effect in the S75 and S85 tests. The prototype tests are based on Froude similitude with a length ratio 1/4 (model/prototype). The corresponding time ratio is 1/2 and the computation duration is 200 h. The spectral significant wave height and peak period are $H_{m0} = 1.04$ m and $T_p = 6.2$ s for the S75P and S85P tests. The till characteristics represented by the values of R_c , f_c , and d_{50} are kept the same in the prototype tests where $H_{m0} = 1.12 - 1.58$ m and $T_p = 4.97 - 5.77$ s in the clay slope test by Wolters et al. (2008). The cross-shore nodal spacing Δx in Table 3.2 is increased to 8 cm.

Figure 4.6 presents the computed cross-shore variation of the sand and clay surface elevations at time $t = 0$ and 200 h. The profile evolution is much more pronounced in the prototype scale because of the increased wave action on the same till as that in the model scale. The sand layer thickness h_p and till erosion rate at time $t = 20, 100, \text{ and } 200$ h are shown in Figures 4.7 and 4.8. The maximum deposited sand height on the eroded till at $t = 200$ h is less than 25 cm. Larger sand deposition resulting from pronounced clay erosion occurs during $t = 0 - 20$ h. The computed erosion rate slowly approaches zero during $t = 100 - 200$ h. The clay bottom is covered with the thicker sand layer.

The cross-shore variations of bedload volume v_{bx} , suspended load volume v_{sx} , and net volume v_x for the S75P and S85P tests in Figures 4.9 and 4.10 are similar to those for the S75 and S85 tests in Figures 4.3 and 4.4. The maximum net cross-shore transport volume is up to $500 \text{ m}^3/\text{m}$ near the shoreline at time $t = 200$ h for the prototype tests due to larger breaking waves and return current. The sand volume budget for the S75P and S85P tests in Table 4.1 indicates large onshore sand transport at $x = 0$. The seaward boundary location $x = 0$ is normally chosen at the location of

limited net sediment transport to minimize its effect on sediment transport in the computation domain as is the case with S75 and S85. The hypothetical prototype tests based on Froude similitude may not be realistic because the initial profile in the zone of $x = 0 - 10$ m in Figure 4.6 is the artificial slope added in the laboratory experiment. It is noted that the calibrated values of $C_a = 2$ and $C_p = 0.5$ in Eq. (2.7) are required to be confirmed in actual prototype tests.

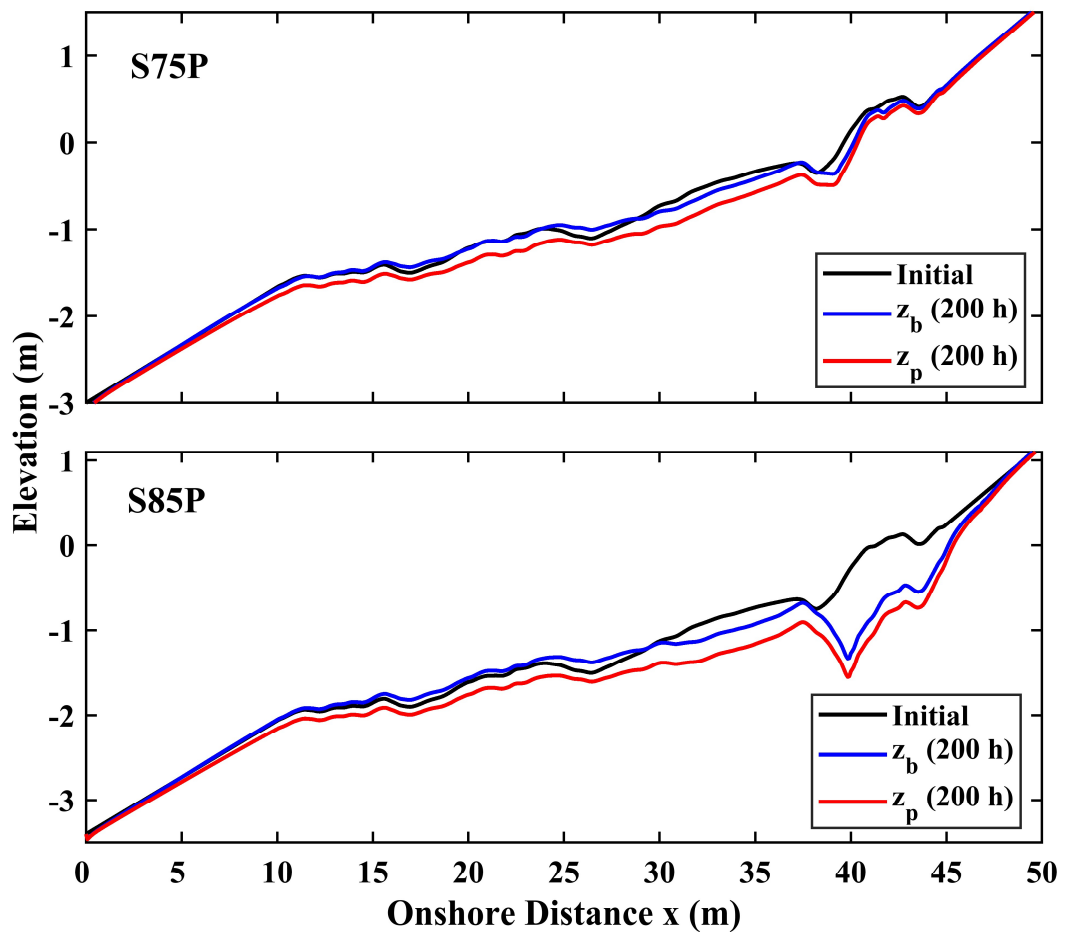


Figure 4.6 Sand surface elevation z_b and clay surface elevation z_p at $t = 0$ and 200 h for S75P and S85P prototype tests

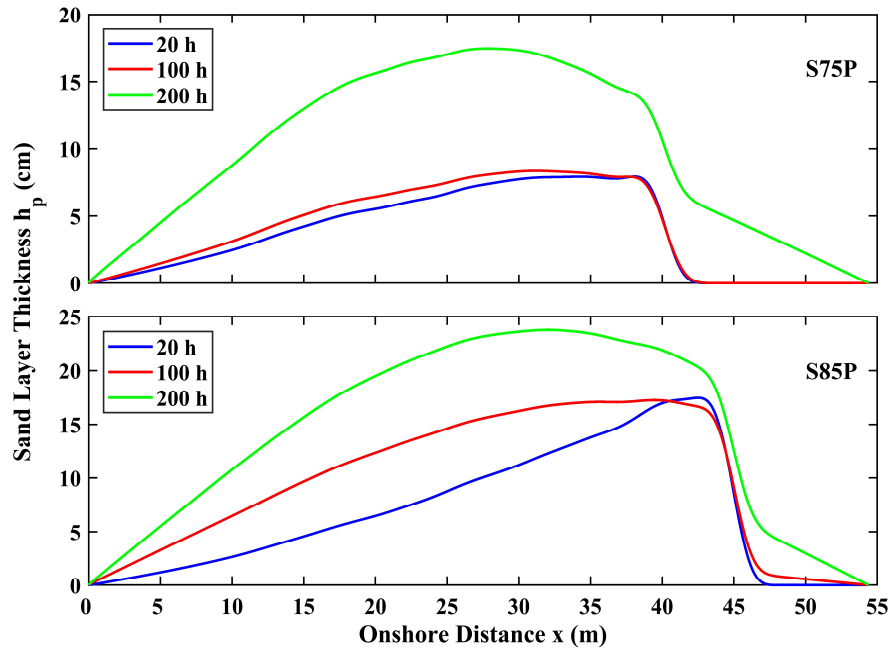


Figure 4.7 Computed sand layer thickness h_p at $t = 20, 100,$ and 200 for S75P and S85P prototype tests

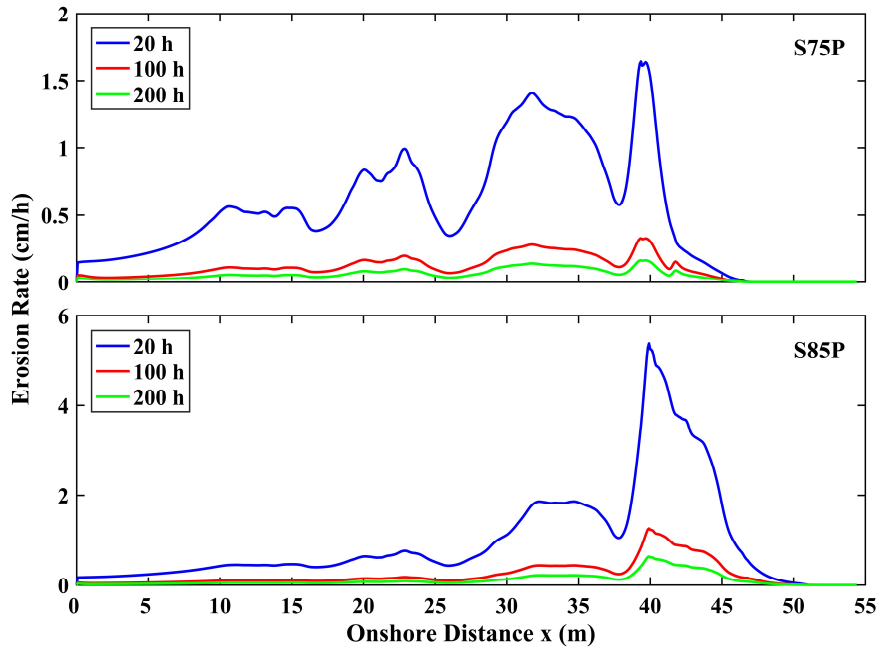


Figure 4.8 Computed erosion rates at $t = 20, 100,$ and 200 for S75P and S85P prototype tests

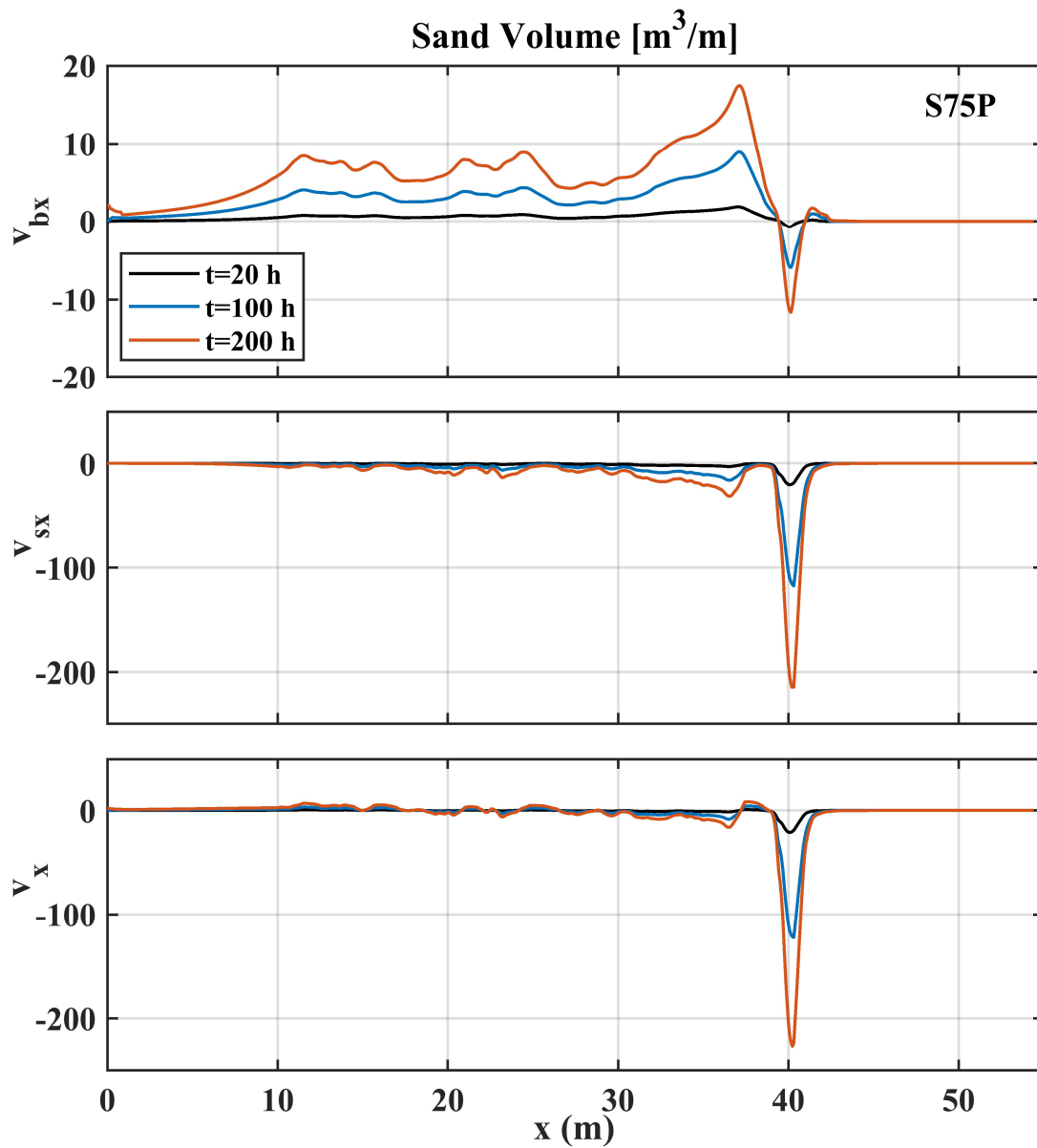


Figure 4.9 Cross-shore sand transport volume v_{bx} , v_{sx} , and v_x (m³/m) at $t = 20, 100,$ and 200 h for S75P prototype test

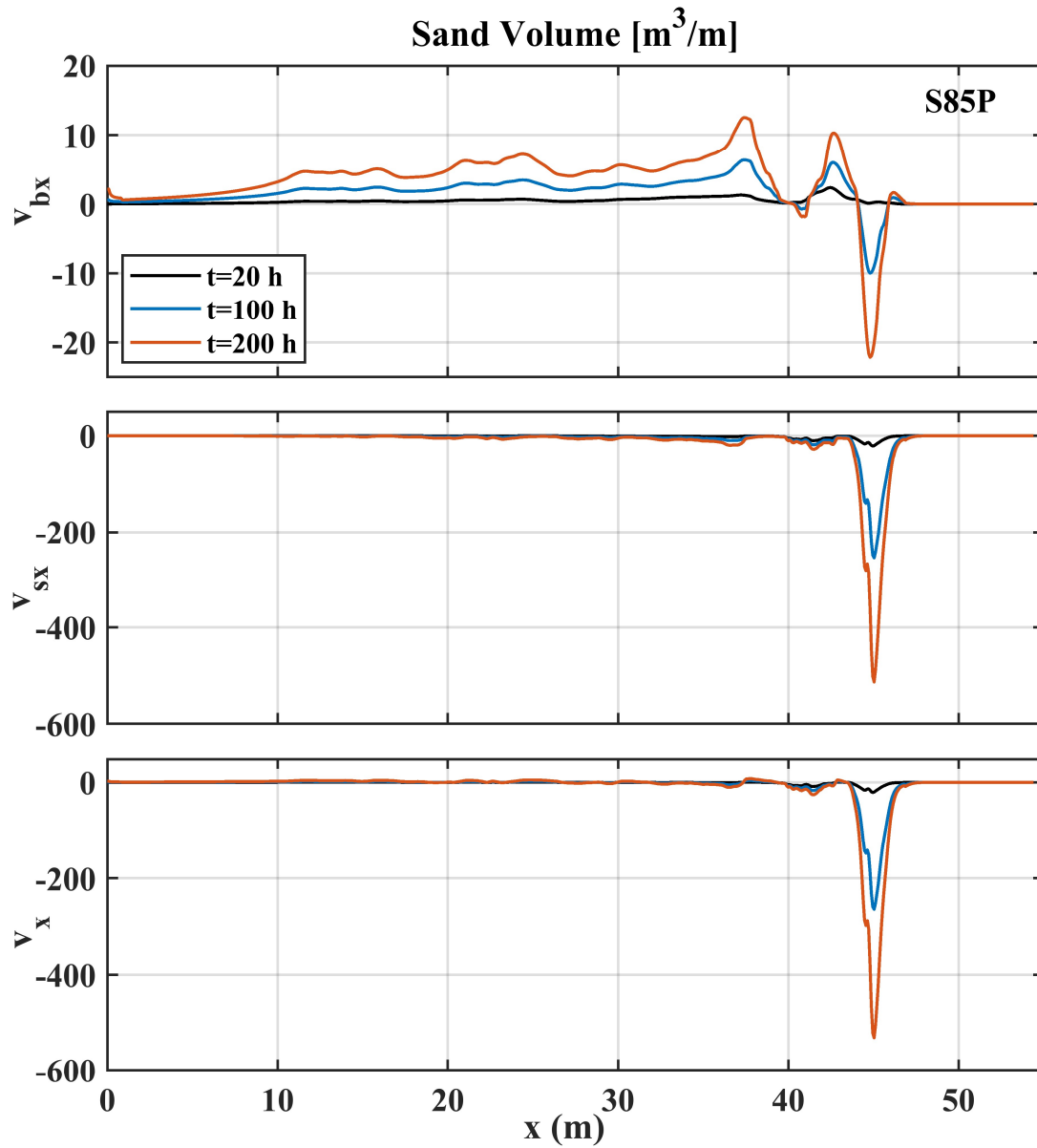


Figure 4.10 Cross-shore sand transport volume v_{bx} , v_{sx} , and v_x (m^3/m) at $t = 20, 100,$ and 200 h for S85P prototype test

4.3 Field Application

The extended CSHORE may be suited for field applications but the clay resistance parameter R_c will need to be calibrated for each field site. It is desirable to correlate R_c with measurable geotechnical parameters. Harris and Whitehouse (2017) reviewed field and laboratory data of scour in cohesive soils around monopoles offshore wind farms and showed that undrained shear strength could be used as a proxy for the erodibility of cohesive soil. Possible applications include the prediction of bluff erosion. Our quantitative understanding of bluff erosion processes is still rudimentary. For example, Payo et al. (2018) reported unexpectedly large bluff recession of 100 m in 14 years along a 900-m coastal stretch after removal of deteriorated wooden structures in front of the bluff. The prediction of steep bluff recession will also require the modeling of bluff failure and sediment supply to the fronting beach [e.g., Ghazian et al. (2018)]. Finally, CSHORE will need to be extended to account for sand supply or removal by longshore and sand transport gradients.

Chapter 5

CONCLUSIONS

The cross-shore numerical model CSHORE was extended to incorporate the basic erosion processes of consolidated cohesive sediment containing some cohesionless sediment (sand for brevity) under irregular breaking waves. The conservation equation of bottom sand was modified to include sand released from the eroding cohesive sediment (clay for brevity). The erosion rate of the clay surface was related to the wave energy dissipation rates caused by wave breaking and bottom friction. The dimensionless function F for the clay surface erosion was introduced to include the abrasive effect of a thin mobile sand layer and the protective effect of a thick sand layer. The dimensional clay resistance parameter and the dimensionless abrasion and protection coefficients were calibrated by comparing the extended CSHORE with available experimental data.

CSHORE was compared with till erosion tests where the till consisted of 21% sand and gravel, and 79% clay and silt. The computed cross-shore wave transformation on the till beach was in fair agreement with the available hydrodynamic data for two tests. The measured and computed till erosion rates were compared for four tests. The overall agreement was reasonable because of the calibration of the clay resistance parameter and the breaker ratio parameter. The detailed cross-shore and temporal variations of the erosion rate was difficult to reproduce consistently, partly because of no measurement of the sand layer thickness before and after each test. The accuracy of the computed sand layer thickness was not evaluated. Furthermore, the till erosion rate of the order of 0.05 cm/h was very small and negligible for a duration of 10 hours or less.

The calibrated CSHORE was applied to compute the till profile evolution for the longer duration of 100 h in two of the four tests to examine the temporal change of the erosion rate resulting from deposition of sand released from the eroded till. The numerical model CSHORE is computational efficient and suited for the prediction of slow cohesive bottom erosion for a long duration. The additional two tests were scaled up on the basis of Froude similitude with a length ratio of 1/4 and the till characteristics were kept the same. The till profile evolution in the two prototype tests was much more pronounced, indicating the need of an experiment of a prototype scale. Sand released from the eroded cohesive bottom moved offshore in the swash zone dominated by suspended sand transport. The sand volume budget was examined to ensure the conservation of sand volume. The calibrated CSHORE will need to be evaluated and improved using actual field data in the future.

REFERENCES

- Bishop, C.T., and Skafel, M.G. 1992. "Detailed description of laboratory tests on the erosion by waves of till profiles." NWRI Contribution No. 92-26, National Water Research Institute, Burlington, Ontario, Canada.
- Bishop, C., Skafel, M., and Nairn, R. 1992. "Cohesive profile erosion by waves." Proc., 23rd Coastal Engineering Conf., ASCE, Reston, VA, 2976-2989.
- Ghazian, M., Farhadzadeh, A., and Khosravi, A. 2018. "Recession of predominantly sandy bluffs." Proc. 36th Coastal Engineering Conf., ASCE, Reston, VA.
- Harris, J.W., and Whitehouse, R.J.S. 2017. "Scour development around large-diameter monopoles in cohesive soils: Evidence from the field." *J. Waterway, Port, Coastal, Ocean Eng.*, 10.1061/(ASCE)WW.1943-5460. 0000414.
- Kamphuis, J.W. 1987. "Recession of glacial till bluffs." *J. Waterway, Port, Coastal, Ocean Eng.*, 113(1), 60-73.
- Kamphuis, J.W. 1990. "Influence of sand or gravel on the erosion of cohesive sediment." *J. Hydraulic Res.*, 28(1), 43-53.
- Kobayashi, N. 2016. "Coastal sediment transport modeling for engineering applications." *J. Waterway, Port, Coastal, Ocean Eng.* 142(6):03116001. [http://doi.org/10.1061/\(ASCE\)WW.1943-5460.0000347](http://doi.org/10.1061/(ASCE)WW.1943-5460.0000347).
- Kobayashi, N., and Weitzner, H. 2015. "Erosion of a seaward dike slope by wave action." *J. Waterway, Port, Coastal, Ocean Eng.*, 10.1061/(ASCE)WW.1943-5460. 0000271, 04014034.
- Kobayashi, N., and Zhu, T., 2017. Bay flooding through tidal inlet and by wave overtopping of barrier beach. *Journal of Waterway, Port, Coastal, and Ocean Engineering* 143, 04017024. [https://doi.org/10.1061/\(ASCE\)WW.1943-5460.0000403](https://doi.org/10.1061/(ASCE)WW.1943-5460.0000403)
- Nairn, R.B., and Southgate, H.N. 1993. "Deterministic profile modelling of nearshore processes. Part 2. Sediment transport and beach profile development." *Coastal Eng.*, 19, 57-96.

- Payo, A., Walkden, M.J.A., Barkwith, A., and Ellis, M.A. 2018. "Modelling rapid coastal catch-up after defense removal along a soft cliff coast of Happisburgh, UK." Proc. 36th Coastal Engineering Conf., ASCE, Reston, VA.
- Skafel, M.G. 1995. "Laboratory measurement of nearshore velocities and erosion of cohesive sediment (till) shorelines." Coastal Eng., 24, 343-349.
- Skafel, M.G., and Bishop, C.T. 1994. "Flume experiments on the erosion of till shore by waves." Coastal Eng., 23, 329-348.
- Trenhaile, A.S., 2009. "Modeling the erosion of cohesive clay coasts." Coastal Eng., 56, 59–72. <https://doi.org/10.1016/j.coastaleng.2008.07.001>
- USACE (US Army Corps of Engineers). 2003. Coastal engineering manual. Washington, DC: USACE.
- Wamsley, T.V., Waters, J.P., and King, D.B. 2011. "Performance of experimental low volume beach fill and clay core dune shore protection project." J. Coastal Res., SI59, 202-210.
- Walkden, M.J.A., and Hall, J.W. 2005. "A predictive mesoscale model of the erosion and profile development of soft rock shores." Coastal Eng., 52, 535-563.
- Wolters, G., Nieuwenhuis, J.W., van der Meer, J., and Klein Breteler, M. 2008. "Large scale tests of boulder clay erosion at the Wieringermeer dike (Ijsselmeer)." Proc. 31st Coastal Engineering Conf., World Scientific, Singapore, 3263-3275.